

# CMS Physics Analysis Summary

---

Contact: cms-pag-conveners-heavyions@cern.ch

2014/05/21

## Femtoscopy with identified charged hadrons in pp, pPb, and peripheral PbPb collisions at LHC energies

The CMS Collaboration

### Abstract

Short range correlations of identified charged hadrons in pp ( $\sqrt{s} = 0.9, 2.76$ , and  $7$  TeV), pPb ( $\sqrt{s_{NN}} = 5.02$  TeV), and peripheral PbPb collisions ( $\sqrt{s_{NN}} = 2.76$  TeV) are studied with the CMS detector at the LHC. Charged pions and kaons at low  $p_T$  and in laboratory pseudorapidity  $|\eta| < 1$  are identified via their energy loss in the silicon tracker. The two-particle correlation functions show effects of quantum statistics, Coulomb interaction, and also indicate the role of multi-body resonance decays and mini-jets. The characteristics of the one-, two-, and three-dimensional correlation functions are studied as a function of the transverse pair momentum and of the charged-particle multiplicity of the event. The extracted radii are in the range 1–5 fm, reaching the highest values for very high multiplicity pPb interactions and for similar multiplicity PbPb collisions. For all systems and multiplicities, the radii decrease with increasing  $k_T$ . The dependence of the radii on the multiplicity and  $k_T$  largely factorizes. For some regions of multiplicity and  $k_T$ , the radii are relatively insensitive to the choice of colliding system and center-of-mass energy.



## 1 Introduction

Measurements of the correlation between hadrons emitted in high energy collisions of nucleons and nuclei can be used to study the spatial extent and shape of the created system. The characteristic radii, the homogeneity lengths, of the particle emitting source can be extracted with reasonable precision [1]. The topic of quantum correlations was well researched in the past by the CMS Collaboration [2, 3] using unidentified charged hadrons produced in  $\sqrt{s} = 0.9, 2.36$ , and  $7 \text{ TeV}$  pp collisions. Those studies only included one-dimensional fits ( $q_{\text{inv}}$ ) of the correlation function. In the meantime the ALICE, PHENIX, and STAR Collaborations have published numerous interesting results on the Bose-Einstein and other femtosscopic (multidimensional) correlations of identified charged hadrons: charged pions [4–8], charged and neutral kaons [9–11], in diverse energy pp, AuAu, and PbPb collisions.

In this paper a study of the short range, low relative momentum, correlations of identified charged hadrons produced in various energy pp, pPb, and PbPb collisions are described. The aim was to look for effects present in pp, pPb, and PbPb interactions using the same analysis methods, producing results as a function of the transverse pair momentum  $k_T$  and of the fully corrected charged-particle multiplicity  $N_{\text{tracks}}$  (in  $|\eta| < 2.4$ ) of the event. In addition, not only charged pions, but also charged kaons (and protons) are studied.

## 2 Data analysis

A detailed description of the CMS (Compact Muon Solenoid) detector can be found in Ref. [12]. The CMS experiment uses a right-handed coordinate system, with the origin at the nominal interaction point (IP) and the z axis along the counterclockwise-beam direction. The pseudorapidity  $\eta$  of a particle (in the laboratory frame) is defined as  $\eta = -\ln[\tan(\theta/2)]$ , where  $\theta$  is the polar angle with respect to the z axis. The central feature of the CMS apparatus is a superconducting solenoid of 6 m internal diameter. Within the 3.8 T field volume are the silicon pixel and strip tracker, the crystal electromagnetic calorimeter, and the brass/scintillator hadron calorimeter. The tracker measures charged particles within the pseudorapidity range  $|\eta| < 2.4$ . It has 1440 silicon pixel and 15 148 silicon strip detector modules, ordered in 13 tracking layers in the  $\eta$  region studied here. In addition to the barrel and endcap detectors, CMS has extensive forward calorimetry. Steel/quartz-fiber forward calorimeters (HF) cover  $3 < |\eta| < 5$ . Beam Pick-up Timing for the eXperiments (BPTX) devices were used to trigger the detector readout. They are located around the beam pipe at a distance of 175 m from the IP on either side, and are designed to provide precise information on the Large Hadron Collider (LHC) bunch structure and timing of the incoming beams.

The analysis methods (event selection, reconstruction of charged particles in the silicon tracker, finding interaction vertices, treatment of pile-up) are identical to the ones used in the previous CMS papers on the spectra of identified charged hadrons produced in  $\sqrt{s} = 0.9, 2.76$ , and  $7 \text{ TeV}$  pp [13] and  $\sqrt{s_{NN}} = 5.02 \text{ TeV}$  pPb collisions [14].

In the case of pPb collisions, due to the asymmetric beam energies, the nucleon-nucleon center-of-mass was not at rest with respect to the laboratory frame but was moving with a velocity  $|\beta| = 0.434$ . Data with shifts in both directions were combined in the analysis.

Complementary to this work, an analysis with unidentified charged hadrons is being pursued by CMS for pp collisions at  $\sqrt{s} = 2.76$  and  $7 \text{ TeV}$ . This alternative extends the previous CMS analysis of one-dimensional correlation functions in terms of  $q_{\text{inv}}$  [2, 3] to the same two- and three-dimensional spaces defined in Section 2.3. The procedure used to find correlation func-

tions for unidentified charged hadrons differs from that described in Section 2.3. In particular, the background reduction without particle identification is performed using double ratios, i.e. by dividing the signal over background ratio obtained with the data by the same ratio from Monte Carlo.

## 2.1 Event selection, reconstruction of charged particles, vertexing

For the present study 8.97, 9.62, and 6.20 M minimum bias events are used from pp collisions at  $\sqrt{s} = 0.9$  TeV, 2.76 TeV, and 7 TeV, respectively, while 8.95 M minimum bias events are available from pPb collisions at  $\sqrt{s_{NN}} = 2.76$  TeV. The data samples are completed by 3.07 M peripheral (60–100%) PbPb events, where 100% corresponds to fully peripheral, 0% means fully central (head-on) collision. The centrality percentages for PbPb are determined via measuring the sum of the energies in the HF calorimeters.

The event selection consisted of the following requirements:

- at the trigger level, the coincidence of signals from both BPTX devices, indicating the presence of both bunches crossing the interaction point; in addition, at least one track with  $p_T > 0.4$  GeV/c in the pixel tracker;
- offline, the presence of at least one tower with energy above 3 GeV in each of the HF calorimeters; at least one reconstructed interaction vertex; beam-halo and beam-induced background events, which usually produce an anomalously large number of pixel hits [15], are suppressed.

The present analysis extends charged particle reconstruction down to  $p_T \approx 0.1$  GeV/c by exploiting special tracking algorithms [16], used in previous studies [13–15, 17], to provide high reconstruction efficiency and low background rate.

The acceptance of the tracker is defined as the fraction of primary charged particles leaving at least two hits in the pixel detector. It is flat in the region  $-2 < \eta < 2$  and  $p_T > 0.4$  GeV/c, and its value is 96–98%. The loss of acceptance at  $p_T < 0.4$  GeV/c is caused by energy loss and multiple scattering of particles, both depending on the particle mass. Likewise, the reconstruction efficiency is about 75–90% at  $p_T > 0.4$  GeV/c, degrading at low  $p_T$ , also in a mass-dependent way. The misreconstructed-track rate is very small, reaching 1% only for  $p_T < 0.2$  GeV/c. The probability of reconstructing multiple tracks from a single true track is about 0.1%, mostly due to particles spiralling in the strong magnetic field of the CMS solenoid. For the range of event multiplicities included in the current study, the efficiencies and background rates do not depend on multiplicity.

The region where collisions occur (beam spot) is measured by reconstructing vertices from many events. Since the bunches are very narrow in the transverse direction, the  $xy$  location of the interaction vertices is well constrained; conversely, their  $z$  coordinates are spread over a relatively long distance and must be determined on an event-by-event basis. The vertex position is determined using reconstructed tracks which have  $p_T > 0.1$  GeV/c and originate from the vicinity of the beam spot, i.e. their transverse impact parameters  $d_T$  satisfy the condition  $d_T < 3\sigma_T$ . Here  $\sigma_T$  is the quadratic sum of the uncertainty in the value of  $d_T$  and the root-mean-square of the beam spot distribution in the transverse plane. An agglomerative vertex-reconstruction algorithm [18] was used, with the  $z$  coordinates (and their uncertainties) of the tracks at the point of closest approach to the beam axis as input. The vertex reconstruction resolution in the  $z$  direction is a strong function of the number of reconstructed tracks, but is always smaller than 0.1 cm. Only tracks associated with a primary vertex are used in the analysis. If multiple vertices are present, the tracks from the highest multiplicity vertex are used. The average

pile-up rate differs from system to system and is below 9%. The probability of merged or split vertices is very small, at or below the per mille level, and the resultant bias is negligible.

The multiplicity of reconstructed tracks,  $N_{\text{rec}}$ , is obtained in the region  $|\eta| < 2.4$ . Over the range  $0 < N_{\text{rec}} < 240$ , the events were divided into 24 classes, defined in Table 1, a region that is well covered by the 60–100% centrality PbPb collisions. To facilitate comparisons with models, the corresponding corrected charged particle multiplicity  $\langle N_{\text{tracks}} \rangle$  in the same acceptance of  $|\eta| < 2.4$  is also determined. For each multiplicity class, the correction from  $N_{\text{rec}}$  to  $\langle N_{\text{tracks}} \rangle$  uses the efficiency estimated with PYTHIA [19] (pp) and HIJING [20, 21] (pPb) simulation in  $(\eta, p_{\text{T}})$  bins. The corrected data are then integrated over  $p_{\text{T}}$ , down to zero yield at  $p_{\text{T}} = 0$  with a linear extrapolation below  $p_{\text{T}} = 0.1$  GeV/c. The yield in the extrapolated region is about 6% of the total yield. The systematic uncertainty due to the extrapolation is small, well below 1%. Finally, the integrals for each eta slice are summed. In the case of PbPb, events generated by the HYDJET 1.8 [22] Monte Carlo event generator (Drum tune), were simulated and reconstructed. The  $N_{\text{rec}} - \langle N_{\text{tracks}} \rangle$  relationship was determined with help of a fourth order polynomial.

## 2.2 Particle identification

The reconstruction of charged particles in CMS is bounded by the acceptance of the tracker and by the decreasing tracking efficiency at low momentum. Particle-by-particle identification using specific ionization is possible in the momentum range  $p < 0.15$  GeV/c for electrons,  $p < 1.15$  GeV/c for pions and kaons, and  $p < 2.00$  GeV/c for protons. In view of the  $(\eta, p_{\text{T}})$  regions where pions, kaons, and protons can all be identified, only particles in the band  $-1 < \eta < 1$  (in the laboratory frame) were used for this measurement.

For the identification of charged particles, the estimated most probable energy loss rate  $\varepsilon$  at a reference path-length  $l_0 = 450 \mu\text{m}$  was used [24]. For an accurate determination of  $\varepsilon$ , the response of all readout chips was calibrated with multiplicative gain correction factors. The procedures for gain calibration and track-by-track determination of  $\varepsilon$  values are the same as they were for the previous analyses [13, 14]. Distributions of  $\ln \varepsilon$  as a function of total momentum  $p$  for positive and negative particles are shown in Fig. 1 in the case of pPb and PbPb

Table 1: Relationship between the number of reconstructed tracks ( $N_{\text{rec}}$ ) and the average number of corrected tracks ( $\langle N_{\text{tracks}} \rangle$ ) in the region  $|\eta| < 2.4$  for the 24 multiplicity classes considered.

$N_{\text{rec}}$	$\langle N_{\text{tracks}} \rangle$			$N_{\text{rec}}$	$\langle N_{\text{tracks}} \rangle$		
	pp	pPb	PbPb		pp	pPb	PbPb
0–9	7	8	7	120–129	142	160	163
10–19	16	19	19	130–139	-	173	177
20–29	28	32	32	140–149	-	185	191
30–39	40	45	45	150–159	-	198	205
40–49	52	58	58	160–169	-	210	219
50–59	63	71	71	170–179	-	222	233
60–69	75	84	84	180–189	-	235	247
70–79	86	96	97	190–199	-	247	261
80–89	98	109	110	200–209	-	260	276
90–99	109	122	123	210–219	-	272	289
100–109	120	135	136	220–229	-	284	302
110–119	131	147	150	230–239	-	296	316

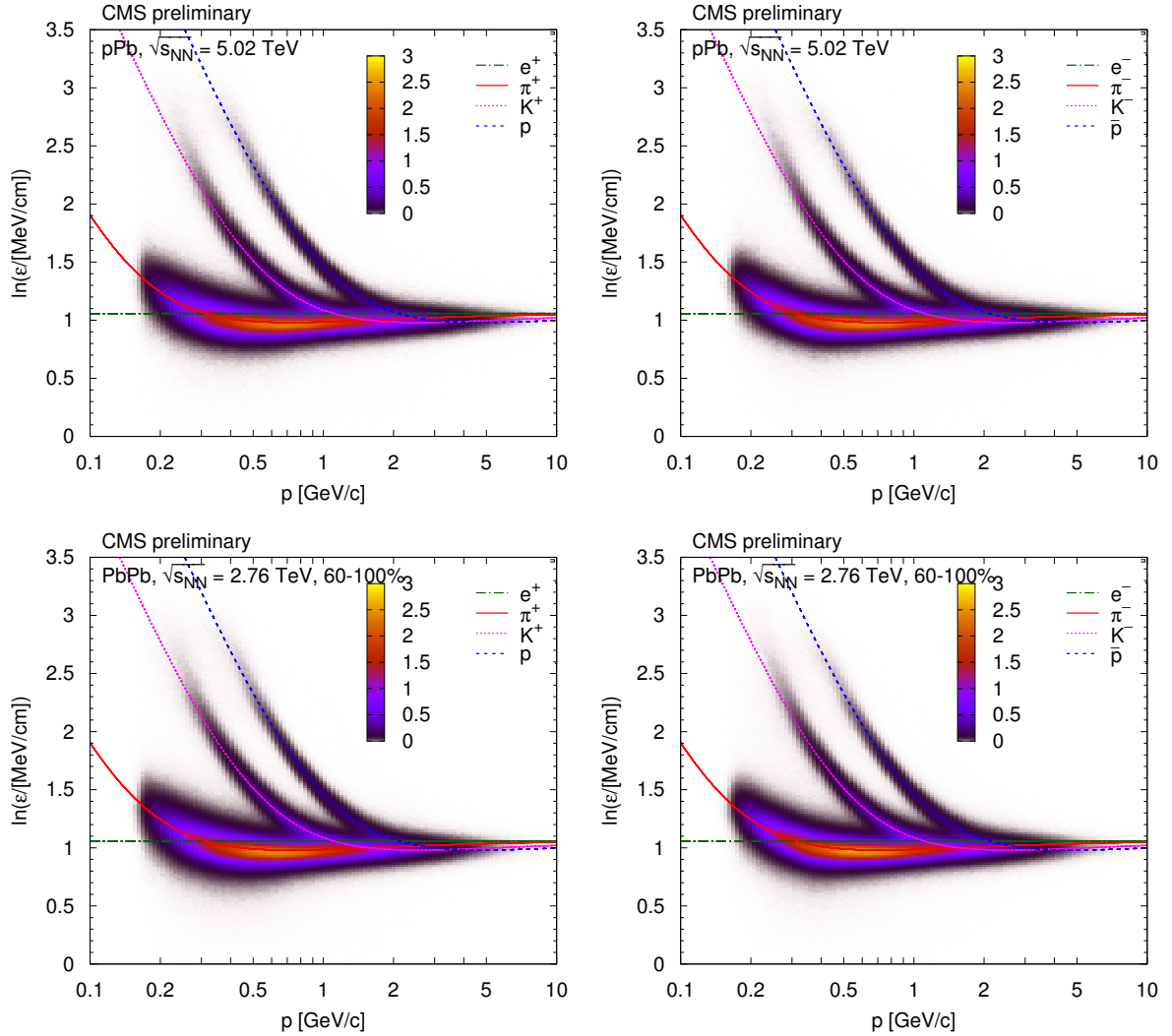


Figure 1: The distribution of  $\ln \varepsilon$  as a function of total momentum  $p$ , for positively (left) and negatively (right) charged particles, in case of pPb collisions at  $\sqrt{s_{NN}} = 5.02 \text{ TeV}$  (top) and PbPb collisions at  $\sqrt{s_{NN}} = 2.76 \text{ TeV}$  (bottom). Here  $\varepsilon$  is the most probable energy loss rate at a reference path length  $l_0 = 450 \mu\text{m}$ . The z scale is shown in arbitrary units and is linear. The curves show the expected  $\ln \varepsilon$  for electrons, pions, kaons, and protons (full theoretical calculation, Eq. (30.11) in Ref. [23]).

collisions. They are compared to the predictions of the energy loss method for electrons, pions, kaons, and protons. The plots for pp interactions are very similar.

Charged particles in the region  $-1 < \eta < 1$  and  $0 < p_T < 2 \text{ GeV}/c$  were sorted into bins with a width of 0.1 units in  $\eta$ , and  $0.05 \text{ GeV}/c$  in  $p_T$ . Since the ratios of particle yields do not change significantly with the charged-particle multiplicity of the event [13, 14], for this purpose the data were not subdivided into bins of  $N_{\text{rec}}$ . The relative abundance of different particle species in an  $(\eta, p_T)$  bin were extracted by minimizing the joint log-likelihood

$$\chi^2 = -2 \sum_{i=\text{tracks}} \ln \left( \sum_{k=\pi, K, p} P_k \exp \left[ -\frac{(\ln \varepsilon_i - \mu_k)^2}{2(\alpha \sigma_i)^2} \right] \right) \quad (1)$$

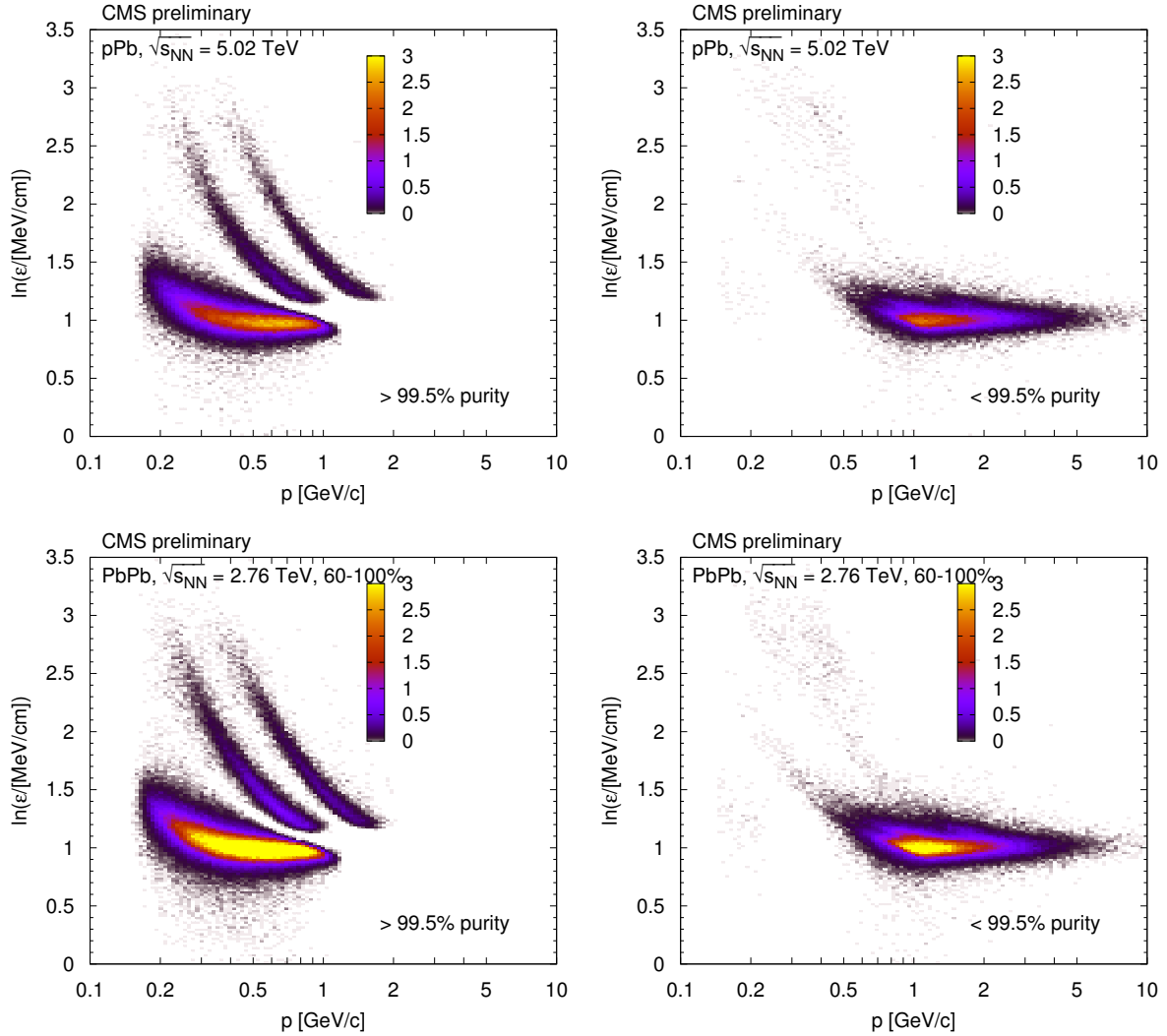


Figure 2: The distribution of  $\ln \varepsilon$  as a function of total momentum  $p$ , for identified charged particles (both charges) with high purity ( $> 99.5\%$ , left) and the rest (right), in case of pPb collisions at  $\sqrt{s_{NN}} = 5.02$  TeV (top) and PbPb collisions at  $\sqrt{s_{NN}} = 2.76$  TeV (bottom).

where  $\mu_k$  are the expected means of  $\ln \varepsilon$  for the different particle species, and  $P_k$  are their relative probabilities. In the above formula  $\varepsilon_i$  and  $\sigma_i^2$  are the estimated most probable value and its variance, respectively. Since the estimated variance can slightly differ from its true value, a scale factor  $\alpha$  was introduced. The  $\mu_k$  values were used to determine a unique  $\ln \varepsilon(p/m)$  function. For the sake of simplicity the collected  $(p/m, \ln \varepsilon)$  pairs, with the corresponding uncertainties, were fitted with a third order polynomial.

In this analysis a very high purity particle identification is performed, since  $P_k / (\sum_{k=\pi,K,p} P_k) > 0.995$  is required. If none of the particle type assumptions yields a  $P_k$  value in this range, the particle is regarded as not identified. This requirement ensures that less than 1% of the examined particle pairs would be fake. The distribution of  $\ln \varepsilon$  as a function of total momentum for identified charged particles with high purity and the rest are shown in Fig. 2, for pPb collisions at  $\sqrt{s_{NN}} = 5.02$  TeV and PbPb collisions at  $\sqrt{s_{NN}} = 2.76$  TeV. The plots for pp interactions are very similar.

### 2.3 Particle pairs, Bose-Einstein correlations

Several types of particle pairs are collected:  $\pi^+\pi^+$ ,  $\pi^-\pi^-$ ,  $\pi^+\pi^-$ ;  $K^+K^+$ ,  $K^-K^-$ ,  $K^+K^-$ . The pair distributions are binned in the number of reconstructed charged particles  $N_{\text{rec}}$  of the event, in the transverse pair momentum  $k_T = |\mathbf{p}_{T,1} + \mathbf{p}_{T,2}|/2$ , and also in the relative momentum ( $\mathbf{q}$ ) variables in the longitudinally co-moving system (LCMS) of the pair. One-dimensional ( $q_{\text{inv}} = |\mathbf{q}|$ ), two-dimensional ( $q_l, q_t$ ), and three-dimensional ( $q_l, q_o, q_s$ ) analyses are performed. Here  $q_o$  is the component of  $\mathbf{q}_t$  parallel to  $\mathbf{k}_T$ ,  $q_s$  is the component of  $\mathbf{q}_t$  perpendicular to  $\mathbf{k}_T$ . The chosen bin-widths for pions and kaons are shown in Table 2.

The construction of the  $\mathbf{q}$  distribution for the “signal” pairs is straightforward: all valid particle pairs from the same event are taken and the corresponding histograms are filled. An ideal “background”  $\mathbf{q}$  distribution should be free of the quantum correlations, but it should properly contain all the rest. This way the ratio of signal and background would give the quantum correlation functions. There are several choices for the construction of the background. We considered the following three prescriptions:

- particles from the actual event are paired with particles from some given number of, in our case 25, preceding events (“event mixing”); only events belonging to the same multiplicity ( $N_{\text{rec}}$ ) class are mixed;
- particles from the actual event are paired, the laboratory momentum vector of the second particle is rotated around the beam axis by 90 degrees (“rotated”);
- particles from the actual event are paired, but the laboratory momentum vector of the second particle is negated (“mirrored”).

Based on the goodness-of-fit distributions (Sec. 8), the event mixing prescription was used while the rotated and mirrored versions, which give worse or much worse  $\chi^2/\text{ndf}$  values, were employed in the estimation of the systematic uncertainty.

The symmetrization of the joint wave function of identical bosons leads to correlations at low values of relative momenta  $q$ . The *measured* two-particle correlation function  $C_2(\mathbf{q})$  is the ratio of signal and background distributions

$$C_2(\mathbf{q}) = \frac{N_{\text{signal}}(\mathbf{q})}{N_{\text{bckgnd}}(\mathbf{q})}, \quad (2)$$

where the background is normalized such that it has the same integral as the signal distribution. The quantum correlation function  $C_{\text{BE}}$ , part of  $C_2$ , is the Fourier transform of the source density distribution  $f(\mathbf{r})$ . There are several possible functional forms that are commonly used to fit  $C_{\text{BE}}$  present in the data: Gaussian  $(1 + \lambda \exp[-(qR)^2/(\hbar c)^2])$  and exponential parametrizations

Table 2: The chosen bin-widths for the various variables studied, shown for pions and kaons.

Variable	Range	Bin-width	
		$\pi$	K
$N_{\text{rec}}$	0–240	10	60
$k_T$ [GeV/c]	0.2–0.7	0.1	0.1
$q_{\text{inv}}$ [GeV/c]	0.0–2.0	0.02	0.04
$q_l, q_t$ [GeV/c]	0.0–2.0	0.04	0.04
$q_l, q_o, q_s$ [GeV/c]	0.0–2.0	0.04	0.04

$(1 + \lambda \exp[-(|q|R)/(\hbar c)])$ , and a mixture of those in higher dimensions. (The denominator  $\hbar c = 0.197 \text{ GeVfm}$  is usually omitted from the formulas, we will also do that in the following.) Factorized forms are particularly popular, such as  $\exp(-q_l^2 R_l^2 - q_o^2 R_o^2 - q_s^2 R_s^2)$  or  $\exp(-q_l R_l - q_o R_o - q_s R_s)$  with some theoretical motivation. The fit parameters are usually interpreted as chaoticity  $\lambda$ , and characteristic radii  $R$ , the homogeneity lengths, of the particle emitting source.

As will be shown in Sec. 3, the exponential parametrization does a very good job in describing all our data. It corresponds to the Cauchy (Lorentz) type source distribution  $f(r) = R/(2\pi^2 [r^2 + (R/2)^2]^2)$ , where  $f$  is normalized,  $\int f(r)d^3r = 1$ . Theoretical studies show that for the class of *stable distributions*, with index of stability  $0 < \alpha \leq 2$ , the Bose-Einstein correlation function has a *stretched exponential* shape [25, 26]. The exponential correlation function implies  $\alpha = 1$ . (The Gaussian would correspond to the special case of  $\alpha = 2$ .) The forms used for the fits are

$$C_{\text{BE}}(q_{\text{inv}}) = 1 + \lambda \exp[-q_{\text{inv}} R], \quad (3)$$

$$C_{\text{BE}}(q_l, q_t) = 1 + \lambda \exp\left[-\sqrt{(q_l R_l)^2 + (q_t R_t)^2}\right], \quad (4)$$

$$C_{\text{BE}}(q_l, q_o, q_s) = 1 + \lambda \exp\left[-\sqrt{(q_l R_l)^2 + (q_o R_o)^2 + (q_s R_s)^2}\right], \quad (5)$$

meaning that the system in multi-dimensions is an ellipsoid with differing radii  $R_l$ ,  $R_t$ , or  $R_l$ ,  $R_o$ , and  $R_s$ . Here  $q_o$  is the component of the transverse relative momentum  $q_t$  parallel to  $k_T$ , while  $q_s$  is the component of  $q_t$  perpendicular to  $k_T$ .

## 2.4 Coulomb interaction

After the removal of the trivial phase space effects (ratio of signal and background distributions), one of the most important source of correlations is the mutual Coulomb interaction of the emitted charged particles. The effect of the Coulomb interaction is taken into account by the factor  $K$ , the squared average of the relative wave function  $\Psi$ , as  $K(q_{\text{inv}}) = \int d^3r f(r) |\Psi(k, r)|^2$ , where  $f(r)$  is the source intensity discussed above. For pointlike source,  $f(r) = \delta(r)$ , and we get the Gamow factor  $G(\eta) = |\Psi(0)|^2 = 2\pi\eta / \exp(2\pi\eta) - 1$ , where  $\eta = \pm\alpha m/q_{\text{inv}}$  is the Landau parameter,  $\alpha$  is the fine-structure constant,  $m$  is the mass of the particle. The positive sign should be used for repulsion (like-sign, ++ or --), and the negative is for attraction (unlike-sign, +-).

For an extended source, a more elaborate treatment is needed [27, 28]. The use of the Bowler-Sinyukov formula [29, 30] is popular. Our data on unlike-sign correlation functions show that while the Gamow factor might give a reasonable description of the Coulomb interaction for pions, it is clearly not enough for kaons. (The possible screening of Coulomb interaction, sometimes seen in data of heavy-ion collisions [31–33], is not considered.) In the  $q$  range studied in this analysis  $\eta \ll 1$  applies. The absolute square of confluent hypergeometric function of the first kind  $F$ , present in  $\Psi$ , can be well approximated as  $|F|^2 \approx 1 + 2\eta \text{Si}(x)$  where  $\text{Si}$  is the sine integral function [34]. Furthermore, for Cauchy type source functions the factor  $K$  is nicely described by the formula  $K(q_{\text{inv}}) = G(\eta) [1 + \pi\eta q_{\text{inv}} R / (1.26 + q_{\text{inv}} R)]$ . In the last step we substituted  $q_{\text{inv}} = 2k$ . The factor  $\pi$  in the approximation comes from the fact that for large  $kr$  arguments  $\text{Si}(kr) \rightarrow \pi/2$ . Otherwise it is a simple but faithful approximation of the result of a numerical calculation, with deviations less than 0.5%.

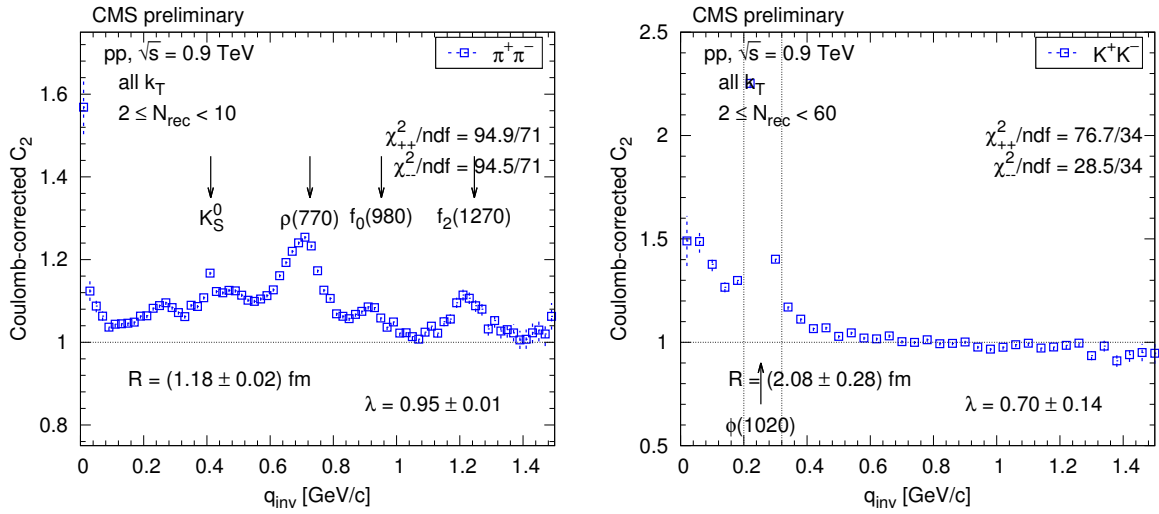


Figure 3: Contribution of resonance decays to the measured Coulomb-corrected correlation function of  $\pi^+\pi^-$  (for  $2 \leq N_{\text{rec}} < 10$ , left, blue open squares) and  $K^+K^-$  (for  $2 \leq N_{\text{rec}} < 60$ , right, blue open squares). The  $\phi(1020)$  peak (right panel) is off-scale.

## 2.5 Clusters: mini-jets, multi-body decays of resonances

The measured unlike-sign correlation functions show contributions from various resonances. Selected Coulomb-corrected correlation functions for low  $N_{\text{rec}}$  bins are shown Fig. 3. The seen resonances include the  $K_S^0$  ( $q_{\text{inv}} = 0.412 \text{ GeV}/c$ ), the  $\rho(770)$  ( $q_{\text{inv}} = 0.726 \text{ GeV}$ ), the  $f_0(980)$  ( $q_{\text{inv}} = 0.925 \text{ GeV}$ ), the  $f_2(1270)$  ( $q_{\text{inv}} = 1.246 \text{ GeV}/c$ ) decaying to  $\pi\mu$ , and the  $\phi(1020)$  ( $q_{\text{inv}} = 0.254 \text{ GeV}/c$ ) decaying to  $K^+K^-$ . Also,  $e^+e^-$  pairs from  $\gamma$  conversions, when misidentified as pion pairs, can appear as a very low  $q_{\text{inv}}$  peak in the  $\pi^+\pi^-$  spectrum. With increasing  $N_{\text{rec}}$  values the effect of resonances diminishes, since their contribution is quickly exceeded by the combinatorics of unrelated particles.

Nevertheless, the Coulomb-corrected unlike-sign correlation functions are not always close to unity at low  $q_{\text{inv}}$ , but show a Gaussian-like hump (Fig. 4). That structure has a varying amplitude but a stable scale ( $\sigma$  of the corresponding Gaussian) of about  $0.4 \text{ GeV}/c$ . This feature is often related to particles emitted inside low momentum mini-jets, but can be also attributed to the effect of multi-body decays of resonances. In the following we will refer to those possibilities as fragmentation of clusters, or *cluster contribution* [35–37]. We have fitted the one-dimensional unlike-sign correlation functions with the following form:

$$C_2^{+-}(q_{\text{inv}}) = c \cdot K^{+-}(q_{\text{inv}}) \left[ 1 + \frac{b}{\sigma_b \sqrt{2\pi}} \exp \left( -\frac{q_{\text{inv}}^2}{2\sigma_b^2} \right) \right] \quad (6)$$

where  $b$  and  $\sigma_b$  are  $N_{\text{rec}}$ - and  $k_{\text{T}}$ -dependent parameters, and  $c$  is a normalization constant. They were successfully parametrized as

$$b(N_{\text{rec}}, k_{\text{T}}) = \frac{b_0}{N_{\text{rec}}^{n_b}} \exp \left( \frac{k_{\text{T}}}{k_0} \right), \quad \sigma_b(N_{\text{rec}}, k_{\text{T}}) = \left[ \sigma_0 + \sigma_1 \exp \left( -\frac{N_{\text{rec}}}{N_0} \right) \right] k_{\text{T}}^{n_T}. \quad (7)$$

The amplitude  $b$  is about inversely proportional with  $N_{\text{rec}}$  (the exponent is  $n_b = 0.80 - 0.96$ ). The parameter  $b_0$  strongly increases with  $\sqrt{s_{\text{NN}}}$ , for pp the dependence can be described as

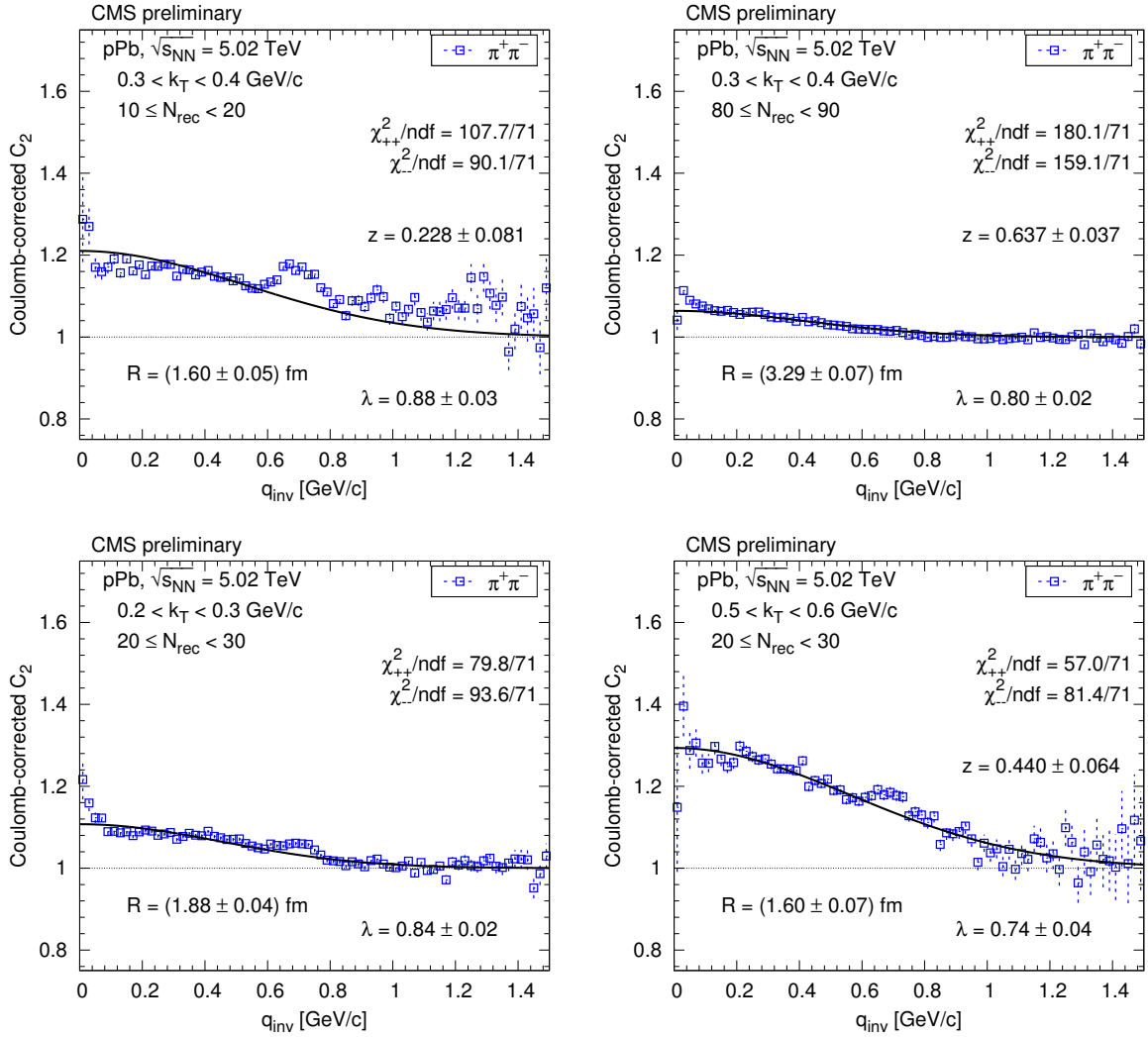


Figure 4: Contribution of clusters (mini-jets and multi-body decays of resonances) to the measured Coulomb-corrected correlation function of  $\pi^+\pi^-$  (blue open squares), for some selected average reconstructed charged track multiplicity bins ( $10 \leq N_{\text{rec}} < 20$ ,  $80 \leq N_{\text{rec}} < 90$ , top), for some selected  $k_T$  bins, for  $20 \leq N_{\text{rec}} < 30$  (bottom), in case of pPb interactions at  $\sqrt{s_{\text{NN}}} = 5.02$  TeV. The solid curves show fits according to Eq. (6).

$0.28 \ln(\sqrt{s}/0.48 \text{ TeV})$ . For pPb  $b_0$  is about 1.6–1.7 times higher than it would be predicted from the pp curve at the same  $\sqrt{s_{\text{NN}}}$ . At the same time  $b$  increases exponentially with  $k_T$ , the parameter  $k_0$  being in the range 1.5–2.5. The Gaussian width  $\sigma_b$  of the hump at low  $q_{\text{inv}}$  first decreases with increasing  $N_{\text{rec}}$ , but for  $N_{\text{rec}} > 70$  remains constant at about 0.35–0.55 GeV/c. The width increases with  $k_T$ , in this case a power-law dependence was appropriate. The expression  $b\sigma_b^2 N_{\text{rec}}$  is proportional to the fraction of particles which have a cluster related partner. Our data show that this fraction does not change substantially with  $N_{\text{rec}}$ , but increases with  $k_T$  and  $\sqrt{s}$  for pp collisions. In summary, the assumed ancestor of this structure, an object, emits particles always in a similar way, with a relative abundance that increases with center-of-mass energy.

The cluster contribution can be also extracted in the case of like-sign correlation function, if the momentum scale of the Bose-Einstein correlation and that of the cluster contribution ( $\approx$

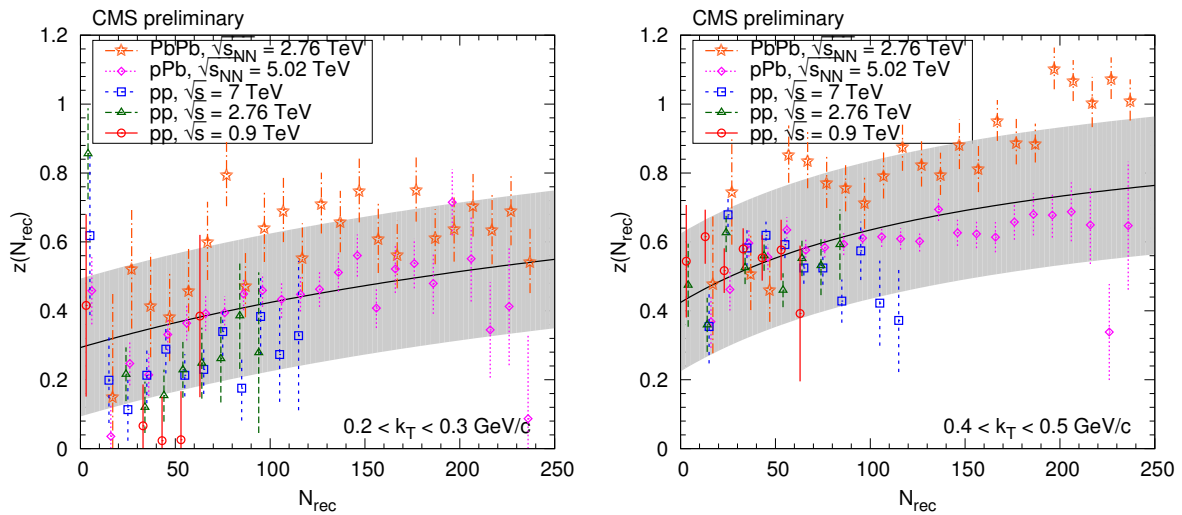


Figure 5: The dependence of the ratio  $z(N_{\text{rec}})$  of the minijet contribution (between like-sign and unlike-sign pairs) as a function of  $N_{\text{rec}}$ , shown here for two  $k_T$  bins studied in this analysis. Fit results (points with error bars) from all collision types are plotted together with combinatorics-motivated fits (solid curves) and their estimated systematic uncertainties ( $\pm 0.2$  bands).

$0.4 \text{ GeV}/c$ ) are different enough. An important element in both mini-jet and multi-body resonance decays is the conservation of electric charge that results in a stronger correlation for unlike-sign pairs than for like-sign pairs. Hence the cluster contribution is expected to be also present for like-sign pairs, with similar shape but a somewhat smaller amplitude. The form of the cluster-related contribution obtained from unlike-sign pairs, but now multiplied by a relative amplitude  $z(N_{\text{rec}}, k_T)$ , is used to fit the like-sign correlations. The dependence of this relative amplitude on  $N_{\text{rec}}$  in  $k_T$  bins is shown in Fig. 5. Results (points with error bars) from all collision types are plotted together with a parametrization  $((aN_{\text{rec}} + b) / (1 + aN_{\text{rec}} + b))$  based on the combinatorics of like-sign and unlike-sign particle pairs (solid curves). Instead of the points, these fitted curves were used to describe the  $N_{\text{rec}}$  dependence of  $z$  in the following. The  $\pm 0.2$  grey bands were chosen to cover most of the points and were used in determining a systematic uncertainty due to the subtraction of the cluster contribution. Thus, the function to fit for like-sign pairs is

$$C_2^{\pm\pm}(q_{\text{inv}}) = c \cdot K^{\pm\pm}(q_{\text{inv}}) \left[ 1 + z(N_{\text{rec}}) \frac{b}{\sigma_b \sqrt{2\pi}} \exp\left(-\frac{q_{\text{inv}}^2}{2\sigma_b^2}\right) \right] C_{\text{BE}}(q_{\text{inv}}). \quad (8)$$

There are about two orders of magnitude less kaon pairs than pion pairs and therefore a detailed study of cluster contribution was not possible. We simply assume that the cluster contribution for kaons is similar to that of pions, and the parametrization deduced for pions with exactly identical parameters is used. This choice is partly justified by unlike-sign kaon correlation functions shown later, but based on the observed difference the systematic uncertainty of  $z(N_{\text{rec}})$  for kaons is increased to 0.3.

In the case of two and three dimensions the measured unlike-sign correlation functions show that instead of  $q_{\text{inv}}$ , the length of the weighted sum of  $q$  components is a better common variable. The Coulomb-corrected unlike-sign correlation functions of pions as a function of a combination of  $q_1$  and  $q_t$ , in some selected  $N_{\text{rec}}$  bins for all  $k_T$  are shown in Fig. 6. A form depending

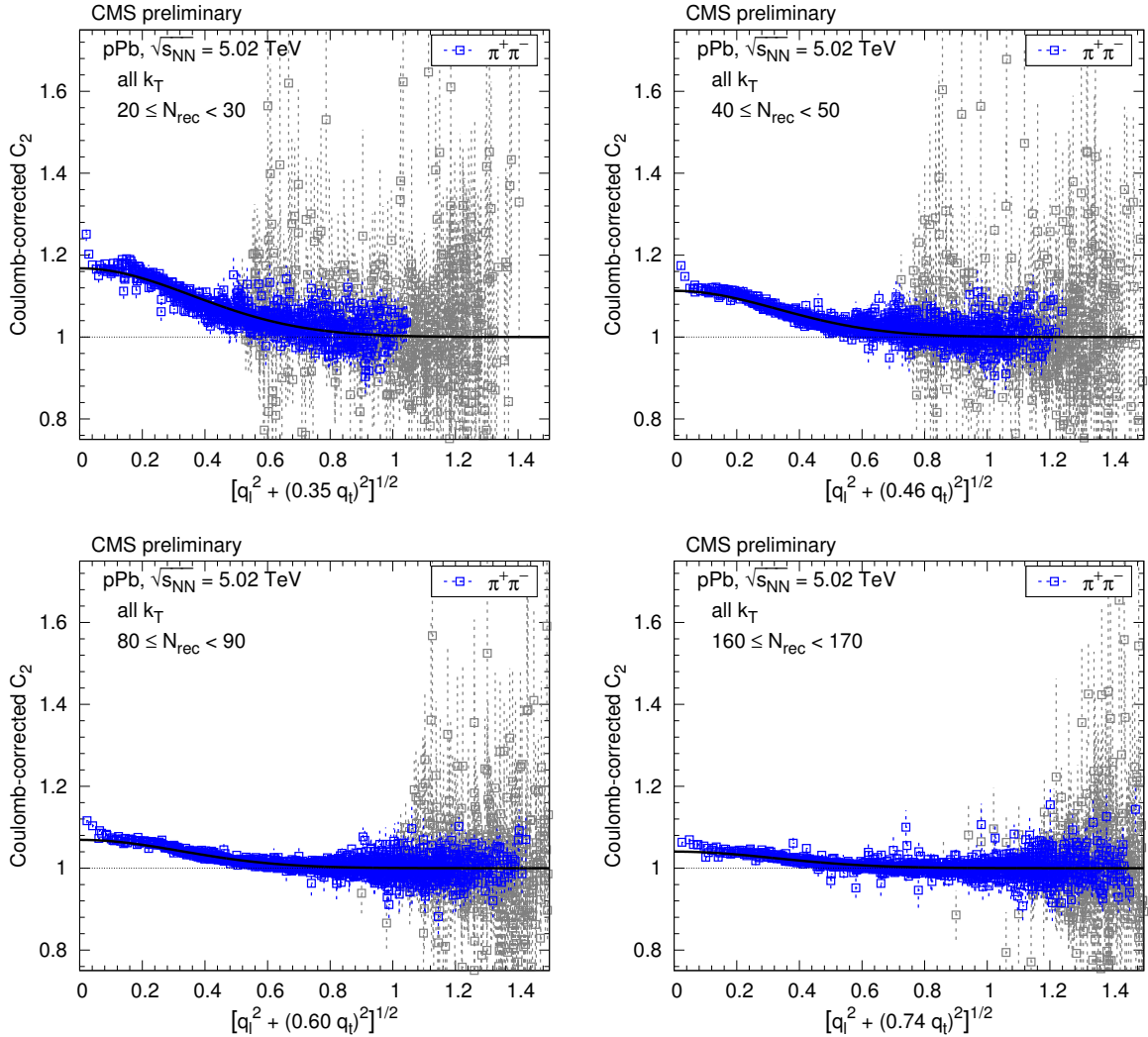


Figure 6: The Coulomb-corrected unlike-sign correlation function of pions (blue squares) as a function of a combination of  $q_l$  and  $q_t$ , in some selected  $N_{\text{rec}}$  bins for all  $k_T$ . Points with relative statistical uncertainty higher than 10% are plotted with light grey color for better visibility. The solid curves indicate the prediction of the parametrized cluster contribution.

on  $q_l$  and  $q_t$  is already sufficient:  $q_h = \sqrt{q_l^2 + (a q_t)^2}$ , where the dependence of the  $a$  factor on  $N_{\text{rec}}$  and  $k_T$  is described as

$$a(N_{\text{rec}}, k_T) = a_0 - b_0 \exp \left( -\frac{N_{\text{rec}}}{N_a} - \frac{k_T}{k_a} \right). \quad (9)$$

(This particular form is motivated by the physics results pointing to an elongated source, shown later.) The corresponding fits, together with those of  $b$  and  $\sigma_b$  are shown in Fig. 7. Instead of the points, these fitted curves were used to describe the  $N_{\text{rec}}$  and  $k_T$  dependence of these parameters in the following. Hence the function to fit for like-sign pairs in the multidimensional case is

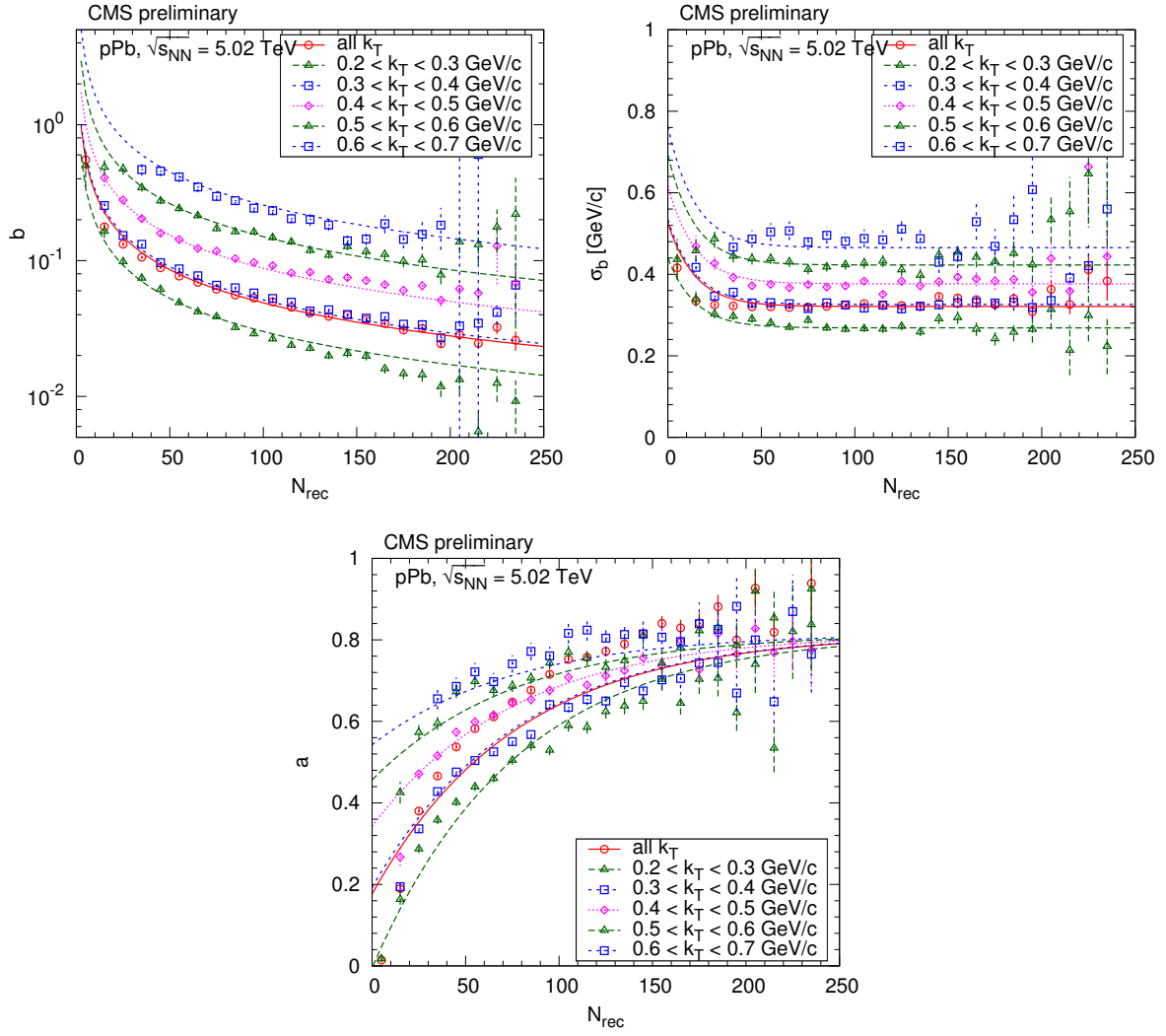


Figure 7: Fitted amplitudes ( $b$ , top left), widths ( $\sigma_b$ , top right), and scale factor ( $a$ , bottom) of the cluster contribution for pPb at  $\sqrt{s_{\text{NN}}} = 5.02 \text{ TeV}$ , studied as a function of the number of reconstructed charged tracks  $N_{\text{rec}}$  in the event and  $k_T$ , for the two-dimensional case ( $q_l, q_t$ ). The curves show the common fits.

$$C_2^{\pm\pm}(\mathbf{q}) = c \cdot K^{\pm\pm}(q_{\text{inv}}) \left[ 1 + z(N_{\text{rec}}) \frac{b}{\sigma_b \sqrt{2\pi}} \exp\left(-\frac{q_h^2}{2\sigma_b^2}\right) \right] C_{\text{BE}}(\mathbf{q}). \quad (10)$$

In the formula above only the normalization  $c$  and the parameters of  $C_2(\mathbf{q})$  are fit, all the other variables (those in  $K$ ,  $z(N_{\text{rec}})$ , also  $b$ ,  $\sigma_b$ ,  $a$ ) were fixed using the parametrizations described above.

## 2.6 Fitting the correlation function

In the case of one dimensional fits of the unlike-sign correlation function, in order to avoid regions with substantial resonance contributions, some relative momentum ranges were not used: for pions  $0.60 < q_{\text{inv}} < 0.80 \text{ GeV}/c$  (due to  $\rho(770)$ ) and  $q_{\text{inv}} < 0.02 \text{ GeV}/c$  (due to photon conversion, misidentified as pair of pions); for kaons  $0.20 < q_{\text{inv}} < 0.32 \text{ GeV}/c$  (due to

$\phi(1020)$ ). Although the probability of reconstructing multiple tracks from a single true track is very small (about 0.1%), in order to avoid regions potentially containing pairs multiply reconstructed tracks, the bin with the smallest  $|q|$  was not used in the like-sign fits.

Since the entries in a counting experiment are Poisson-distributed, the corresponding log-likelihood to minimize is  $\chi^2 = \sum_i 2 [t_i - y_i + y_i \log(y_i/t_i)]$ . In order to speed up computations during histogram fitting, the log term is replaced by a rational function, that is, a ratio of two polynomials. It is very well approximated as  $\log x \approx 2(x-1)/(x+1)$ , the deviations are smaller than 4% in the region  $1/2 < x < 2$ . With that the approximate merit function is  $\chi^2 \approx \sum_i 2(y_i - t_i)^2/(y_i + t_i)$ . Note that it is just between Pearson's and Neyman's  $\chi^2$  formulas.

The distribution of  $\chi^2/\text{ndf}$  values of the correlation function fits for mixed event, opposite, rotated background are shown in Fig. 8. While the mixed event prescription gives reasonable  $\chi^2/\text{ndf}$  distributions in all cases, the opposite prescription is clearly worse, and the rotated prescription gives the worst results. A selection of correlation functions and fits are shown in Figs. 9–13.

The correlation functions corrected for Coulomb and cluster contributions show a minimum around  $0.5 \text{ GeV}/c$ , but the amplitude of this very shallow depression is only about 1%. A similar dip, with a larger amplitude, was already seen in previous CMS analyses [2, 3] where a different procedure was used to remove the cluster contribution. We cannot expect perfect cancellation of various signal and background contributions over all  $q$ . Therefore, in this analysis we do not study this structure further, but concentrate on the major features of the correlation function.

## 2.7 Systematic uncertainties

The systematic uncertainties are dominated by two sources: the dependence of the final results on the way the background distribution is constructed, and the uncertainties of the amplitude  $z$  of the cluster contribution for like-sign pairs with respect to those for unlike-sign ones.

Several choices for the construction of the background distribution were studied. The goodness-of-fit distributions clearly favored the event mixing prescription, while the rotated version gave worse values, the mirrored prescription having the worst performance. The associated systematic uncertainty was calculated by performing the analysis all the way to the end using the mixed event and the rotated variant, and calculating the root-mean-square of the final results (radii and  $\lambda$ ).

Although the dependence of the ratio of the minijet contribution  $z$  (between like-sign and unlike-sign pairs) as a function of  $N_{\text{rec}}$  could be well described by theory-motivated fits in all  $k_T$  regions, the extracted ratios show some deviations within a system, and also between systems. In order to cover those variations, the analysis was performed by moving the fitted ratio up and down by 0.2 for pions, and by 0.3 for kaons. The associated systematics were calculated by taking the average distance of the final results (radii and  $\lambda$ ) from their central values.

The differences between positively and negatively charged pions were found to be small and consistent with each other within the statistical uncertainties. Thus, no additional systematics were associated. The much lower number of kaons pairs forced us to treat them together, the large statistical uncertainties did not allow for a differential study. Nevertheless no deviations between  $K^+$  and  $K^-$  are seen in the data, they are compatible within the statistical uncertainties of the measurements.

In order to suppress the effect of multiply reconstructed particles and misidentified photon conversions, the low  $q$  region had to be excluded from the fits. To study the sensitivity of the

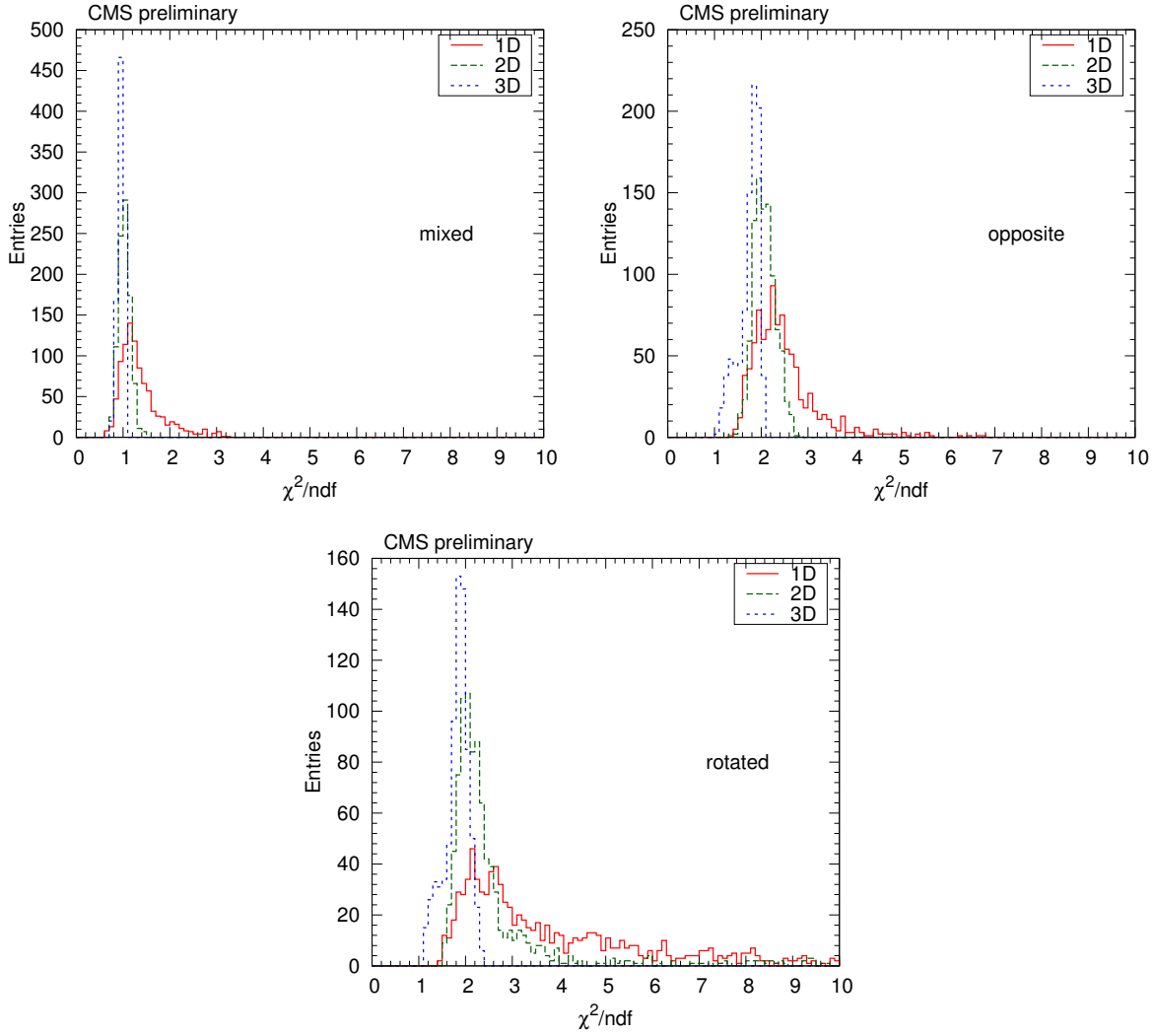


Figure 8: Distribution of  $\chi^2/\text{ndf}$  values of the correlation function fits for mixed event, opposite, and rotated background, for one-, two-, and three-dimensional fits. Each entry in the histograms represents a fit for a system, in a  $N_{\text{rec}}$  and  $k_T$  bin.

results to the size of the excluded range, its higher limit was doubled and tripled. Both the radii and  $\lambda$  decreased slightly with increasing exclusion region. As a result, the contribution of this effect to systematic uncertainty was estimated to be 0.1 fm for the radii and 0.05 for the  $\lambda$ .

The systematic uncertainties from various sources were added in quadrature.

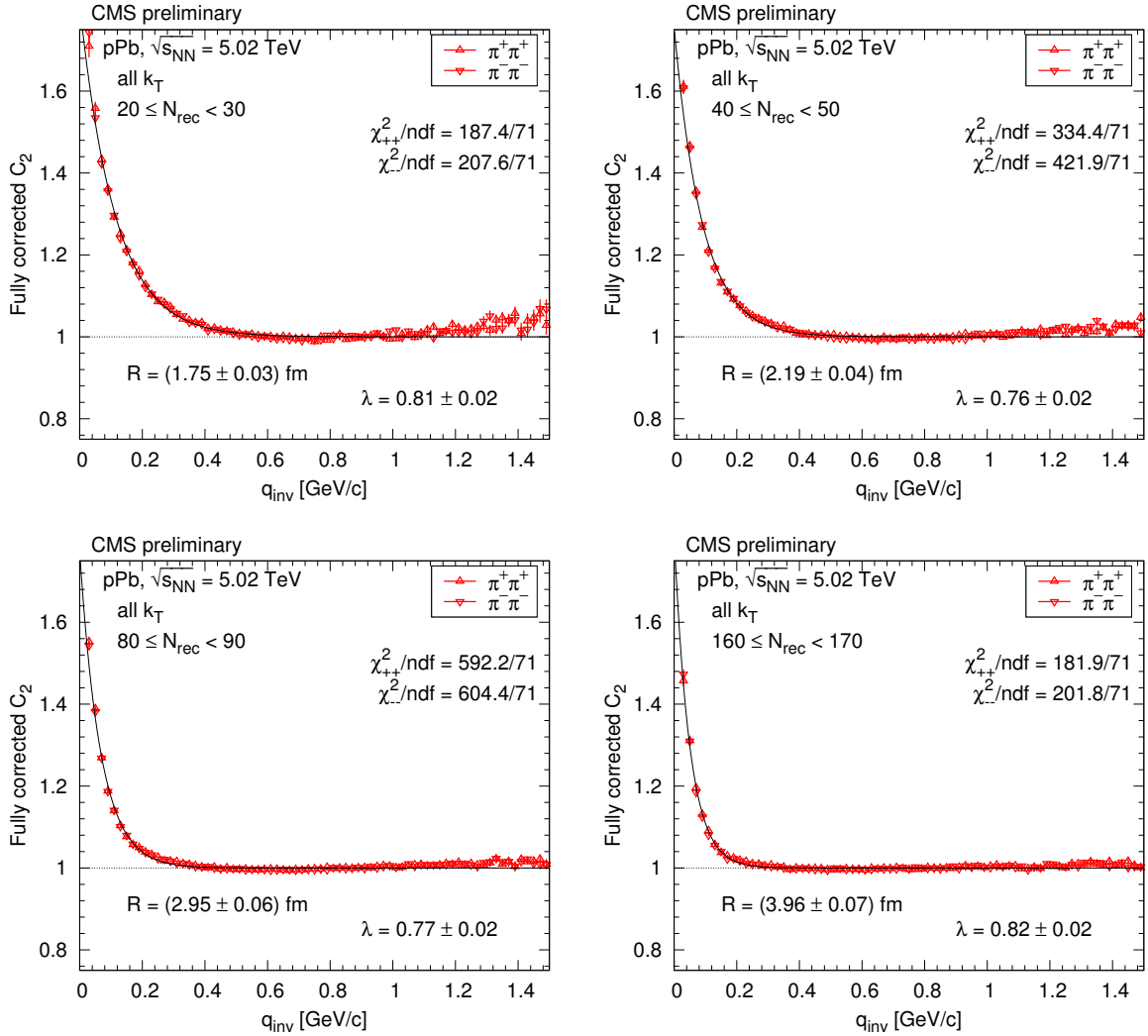


Figure 9: The like-sign correlation function of pions (red triangles) corrected for Coulomb interaction and cluster contribution (mini-jets and multi-body resonance decays) as a function of  $q_{\text{inv}}$ , in some selected  $N_{\text{rec}}$  bins for all  $k_T$ . The solid curves indicate fits with the exponential Bose-Einstein parametrization.

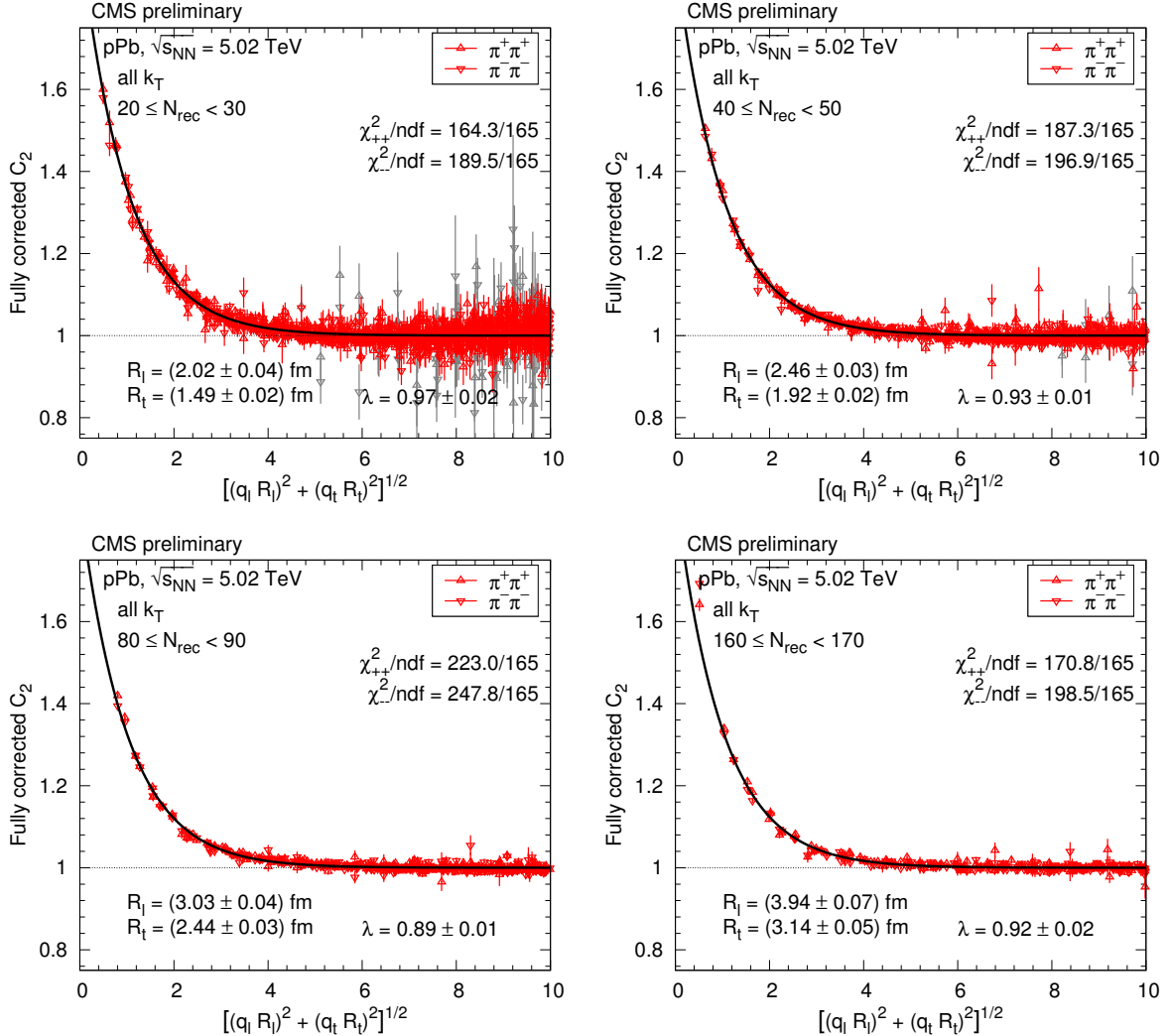


Figure 10: The like-sign correlation function of pions (red triangles) corrected for Coulomb interaction and cluster contribution (mini-jets and multi-body resonance decays) as a function of the combined momentum, in some selected  $N_{\text{rec}}$  bins for all  $k_T$ . Points with relative statistical uncertainty higher than 10% are plotted with light grey color for better visibility. The solid curves indicate fits with the exponential Bose-Einstein parametrization.

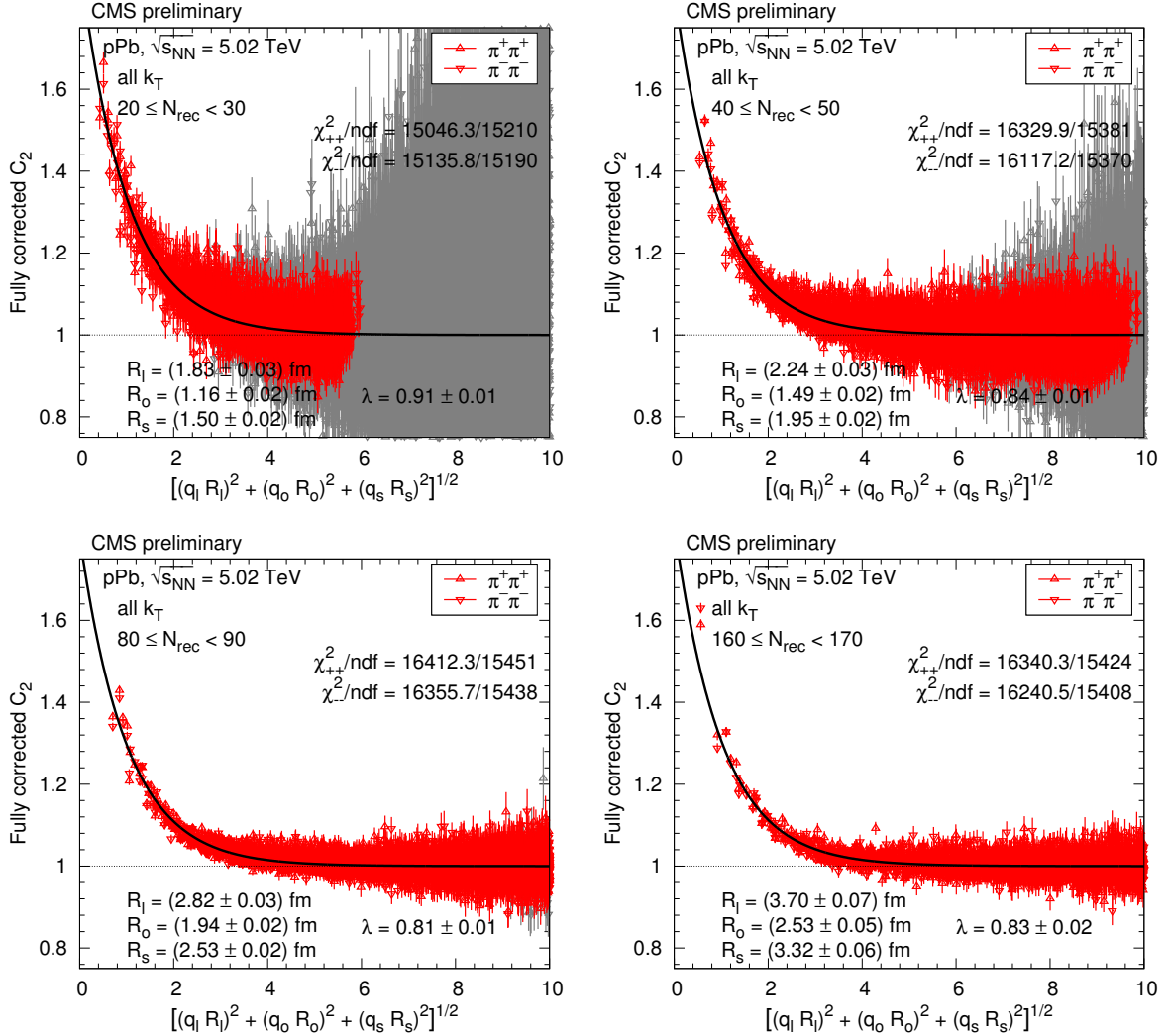


Figure 11: The like-sign correlation function of pions (red triangles) corrected for Coulomb interaction and cluster contribution (mini-jets and multi-body resonance decays) as a function of the combined momentum, in some selected  $N_{\text{rec}}$  bins for all  $k_T$ . Points with relative statistical uncertainty higher than 10% are plotted with light grey color for better visibility. The solid curves indicate fits with the exponential Bose-Einstein parametrization.

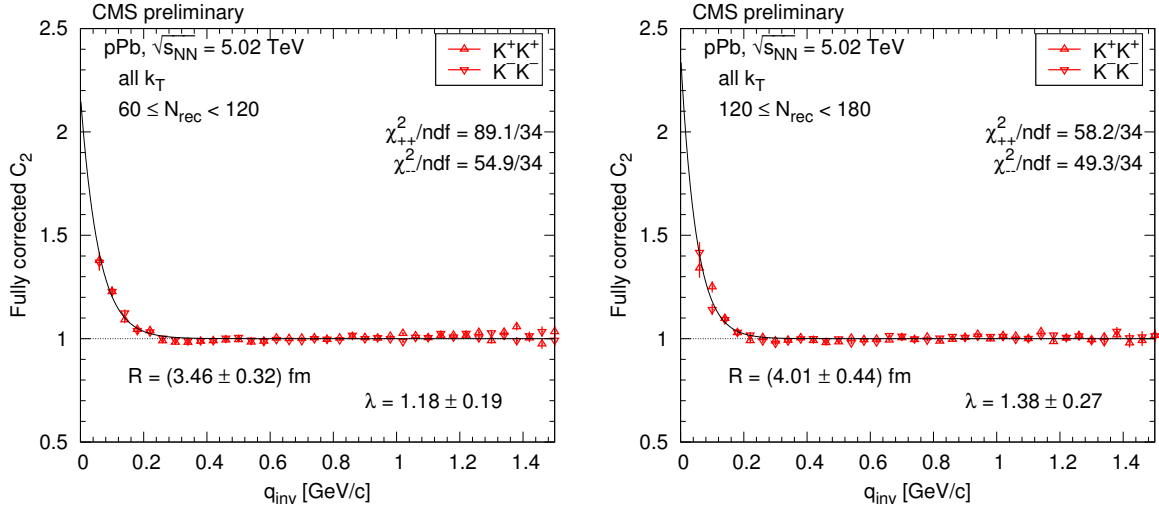


Figure 12: The like-sign correlation function of kaons (red triangles) corrected for Coulomb interaction and cluster contribution (mini-jets and multi-body resonance decays) as a function of  $q_{\text{inv}}$ , in some selected  $N_{\text{rec}}$  bins for all  $k_T$ . The solid curves indicate fits with the Bose-Einstein parametrization.

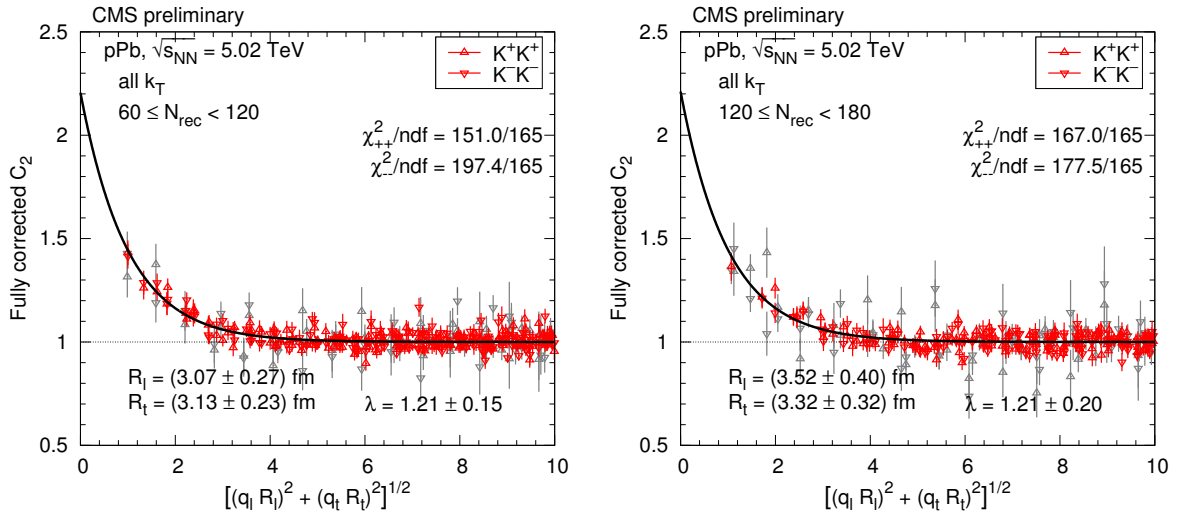


Figure 13: The like-sign correlation function of kaons (red triangles) corrected for Coulomb interaction and cluster contribution (mini-jets and multi-body resonance decays) as a function of the combined momentum, in some selected  $N_{\text{rec}}$  bins for all  $k_T$ . Points with relative statistical uncertainty higher than 10% are plotted with light grey color for better visibility. The solid curves indicate fits with the exponential Bose-Einstein parametrization.

### 3 Results

The characteristics of the extracted one-, two-, and three-dimensional correlation functions as a function of the transverse pair momentum  $k_T$  and of the charged-particle multiplicity  $N_{\text{tracks}}$  (in the range  $|\eta| < 2.4$  in the laboratory frame) of the event are presented here. In all the following plots (Figs. 14–27), the results of positively and negatively charged hadrons are averaged. For clarity, values and uncertainties of the neighboring  $N_{\text{tracks}}$  bins were averaged two by two, and only the averages are plotted. The central values of radii and chaoticity parameter  $\lambda$  are given by markers. The statistical uncertainties are indicated by vertical error bars, the combined systematic uncertainties (choice of background method; uncertainty of the relative amplitude  $z$  of the cluster contribution; low  $q$  exclusion) are given by open boxes. Unless indicated, the lines are drawn to guide the eye (cubic splines whose coefficients are found by weighing the data points with the inverse of their squared statistical uncertainty).

The  $N_{\text{tracks}}$  dependence of the one-dimensional radius and chaoticity parameter for pions, in several  $k_T$  bins, for all studied systems are shown in Figs. 14 and 15. The one-dimensional radii found for pions from proton-proton collisions span a similar range to those found previously [2, 3]. Similar results for kaons are displayed in Figs. 16 and 17. The  $N_{\text{tracks}}$  dependence of the two-dimensional radii and the corresponding chaoticity parameters for pions, in several  $k_T$  bins, for all studied systems are shown in Figs. 18 and 19. The  $k_T$  dependence of one- and two-dimensional radii for pions, in several  $N_{\text{rec}}$  bins, for all systems studied are shown in Fig. 20. The  $N_{\text{tracks}}$  dependence of the three-dimensional radii and the corresponding chaoticity parameters for pions, in several  $k_T$  bins, for all studied systems are shown in Figs. 21–24. The  $k_T$  dependence of three-dimensional radii for pions, in several  $N_{\text{rec}}$  bins, for all systems studied is shown in Fig. 25.

The  $N_{\text{tracks}}$  dependence of the one-dimensional pion radius is remarkably similar for pp and pPb in all  $k_T$  bins. The similarity also applies to PbPb if  $k_T > 0.4 \text{ GeV}/c$ . The  $N_{\text{tracks}}$  dependence of two-dimensional pion radii,  $R_l$  and  $R_t$ , is similar for pp and pPb in all  $k_T$  bins. In general  $R_l > R_t$ , the source is elongated in the beam direction. In the case of PbPb  $R_l \approx R_t$ , the source is quite symmetric. Also, three-dimensional pion radii show a similar pattern.  $R_l$ ,  $R_o$ , and  $R_t$  are similar for pp and pPb in all  $k_T$  bins. In general  $R_l > R_s > R_o$ , the source is again elongated in the beam direction. In the case of PbPb  $R_l \approx R_o \approx R_s$ , the source is symmetric. In addition, PbPb data show a slightly different  $N_{\text{tracks}}$  dependence.

The  $R_l$  radii extracted from the two- and three-dimensional fits slightly differ. While they are the same within statistical uncertainties for pp at  $\sqrt{s} = 0.9 \text{ TeV}$ , the three-dimensional radii are on average smaller by 0.15 fm for pp at  $\sqrt{s} = 2.76 \text{ TeV}$ , by 0.3 fm for pp at  $\sqrt{s} = 7 \text{ TeV}$  and pPb at  $\sqrt{s_{NN}} = 5.02 \text{ TeV}$ , and by 0.5 fm for PbPb at  $\sqrt{s_{NN}} = 2.76 \text{ TeV}$ .

The pion  $\lambda$  values are usually below one, in the range 0.7–1, and seem to be approximately the same function of  $N_{\text{tracks}}$  for all systems and  $k_T$  bins. The one-dimensional kaon radius increases with  $N_{\text{tracks}}$ , but with a smaller slope than seen for pions. Since we measure the size of the system at the last interactions, resonances and rescattering may play a role here.

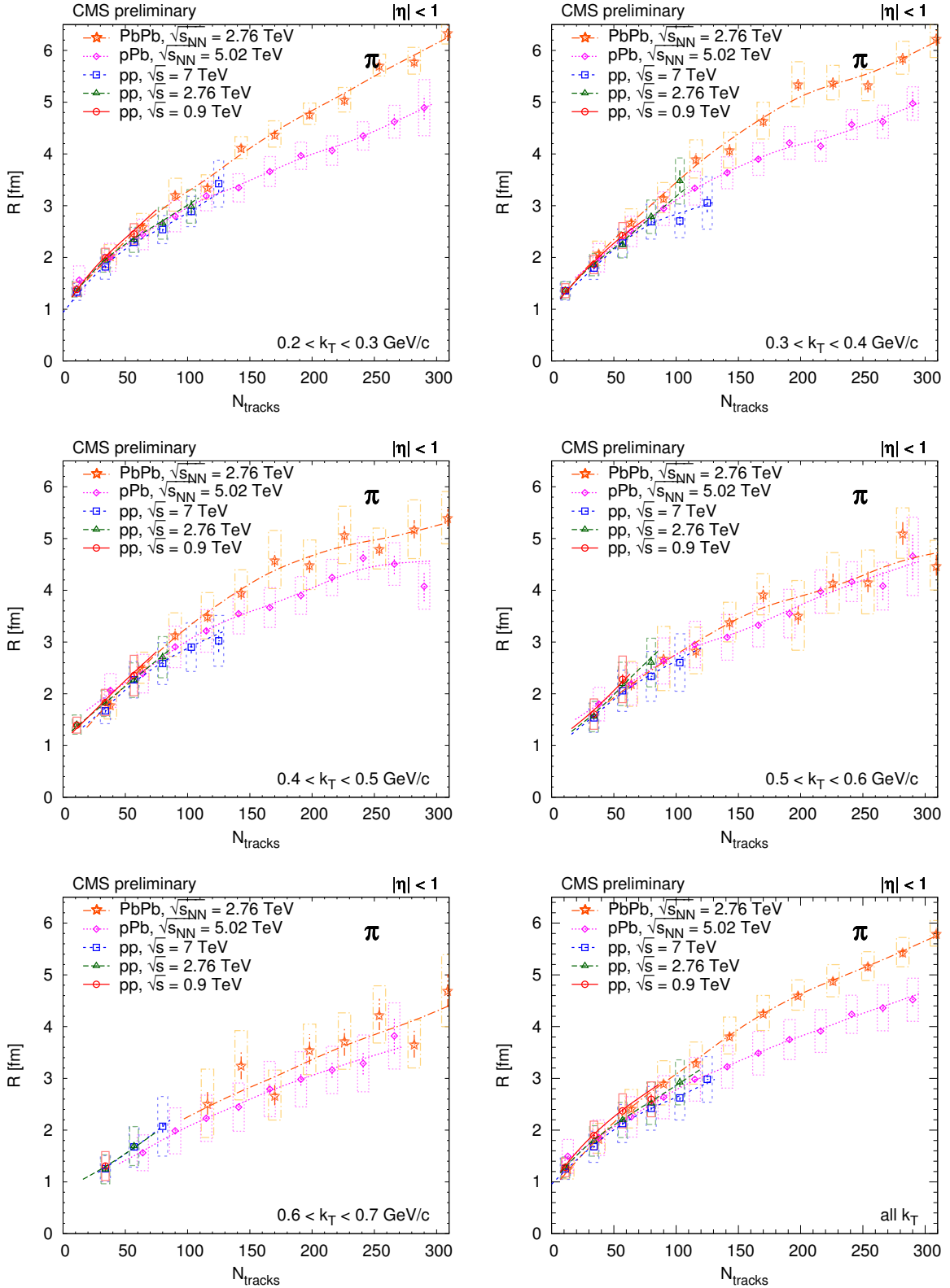


Figure 14:  $N_{\text{tracks}}$  dependence of the one-dimensional pion radius, shown here for several  $k_T$  bins, for all studied reactions. Lines are drawn to guide the eye.

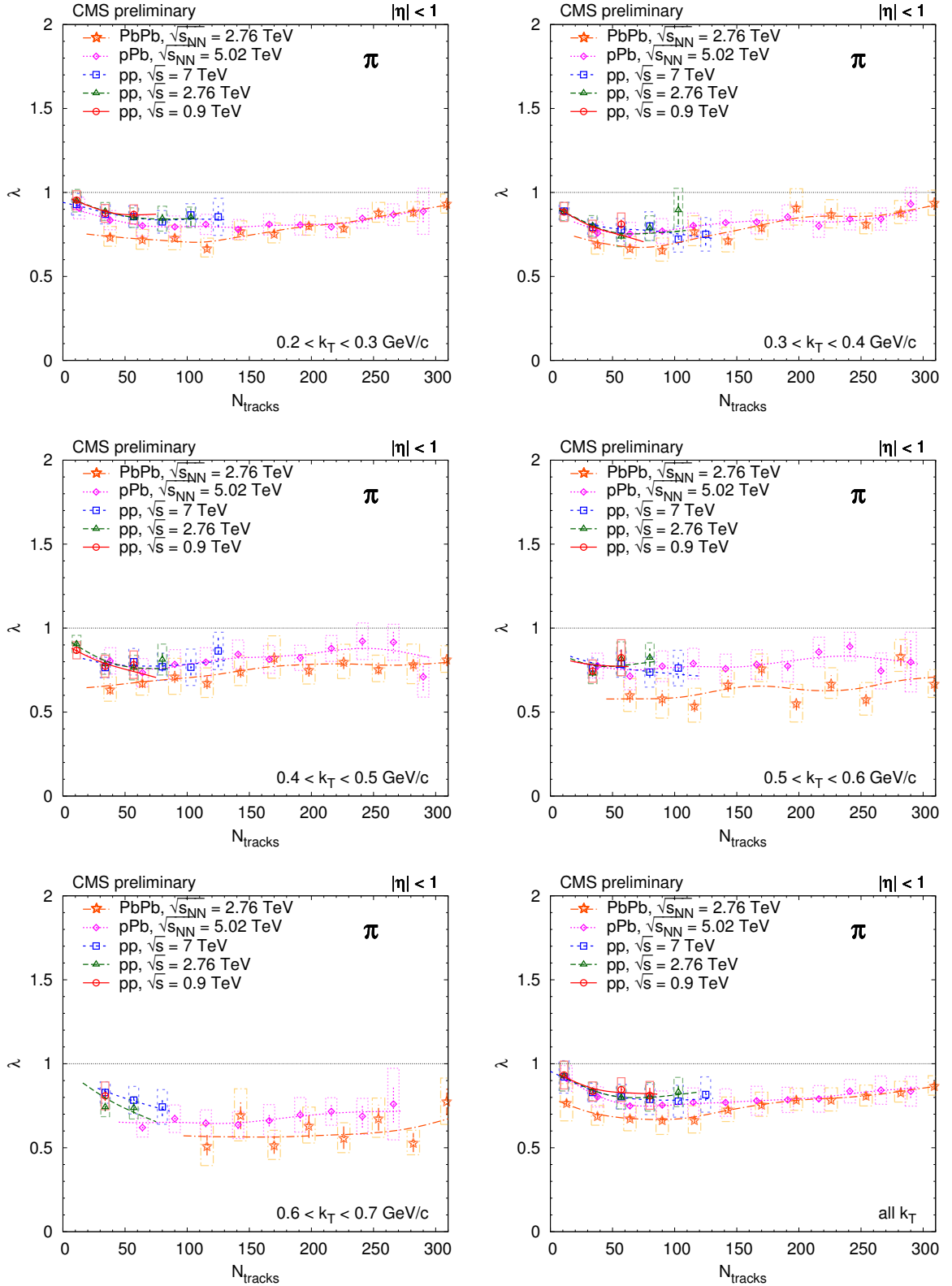


Figure 15:  $N_{\text{tracks}}$  dependence of the one-dimensional pion chaoticity parameter, shown here for several  $k_T$  bins, for all studied reactions. Lines are drawn to guide the eye.

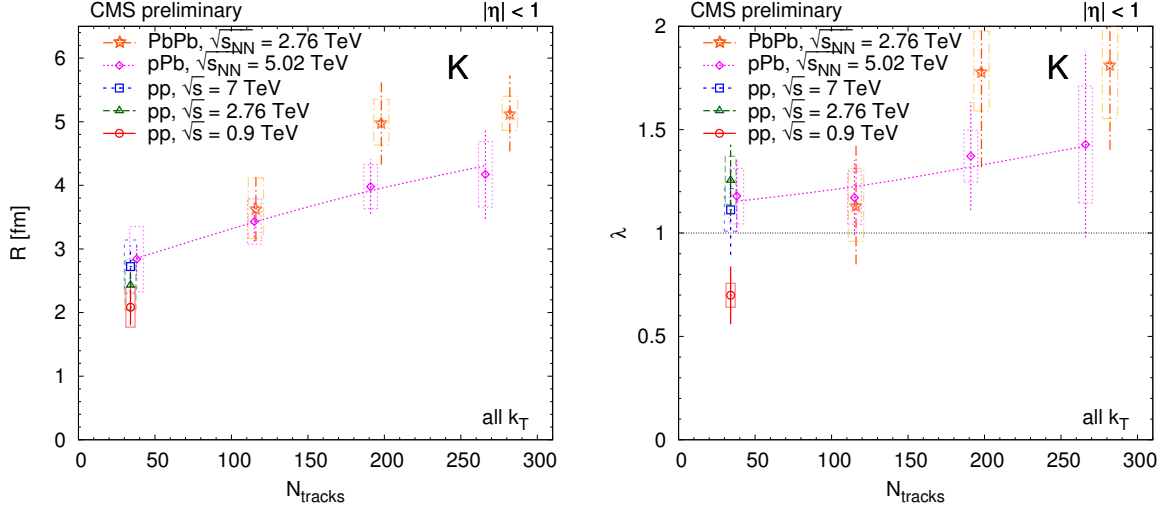


Figure 16:  $N_{\text{tracks}}$  dependence of the one-dimensional kaon radius (left) and chaoticity parameter (right). Lines are drawn to guide the eye.

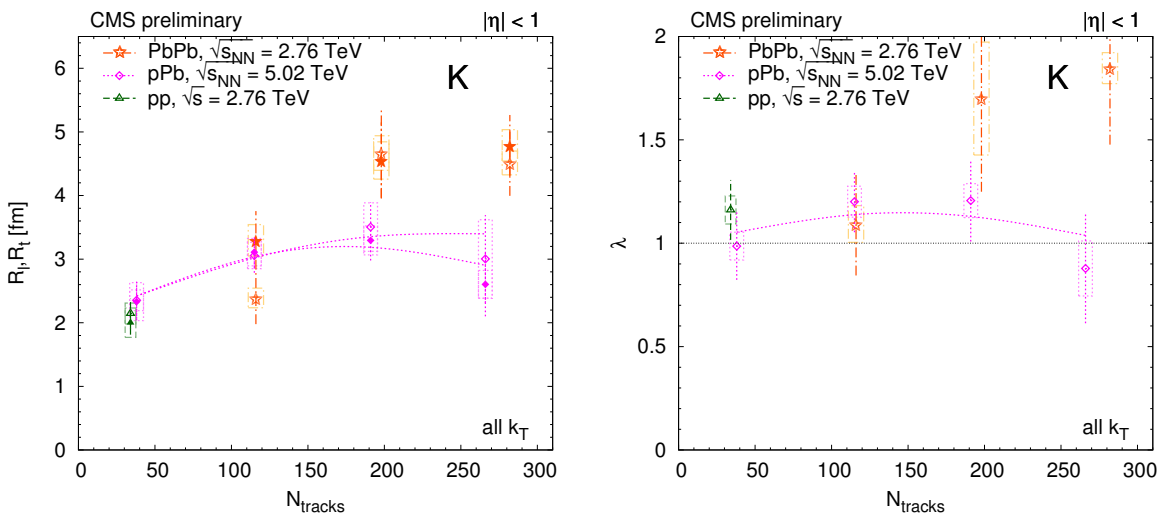


Figure 17:  $N_{\text{tracks}}$  dependence of the two-dimensional kaon radii (left;  $R_l$  – open symbols,  $R_t$  – closed symbols) and chaoticity parameter (right). Lines are drawn to guide the eye.

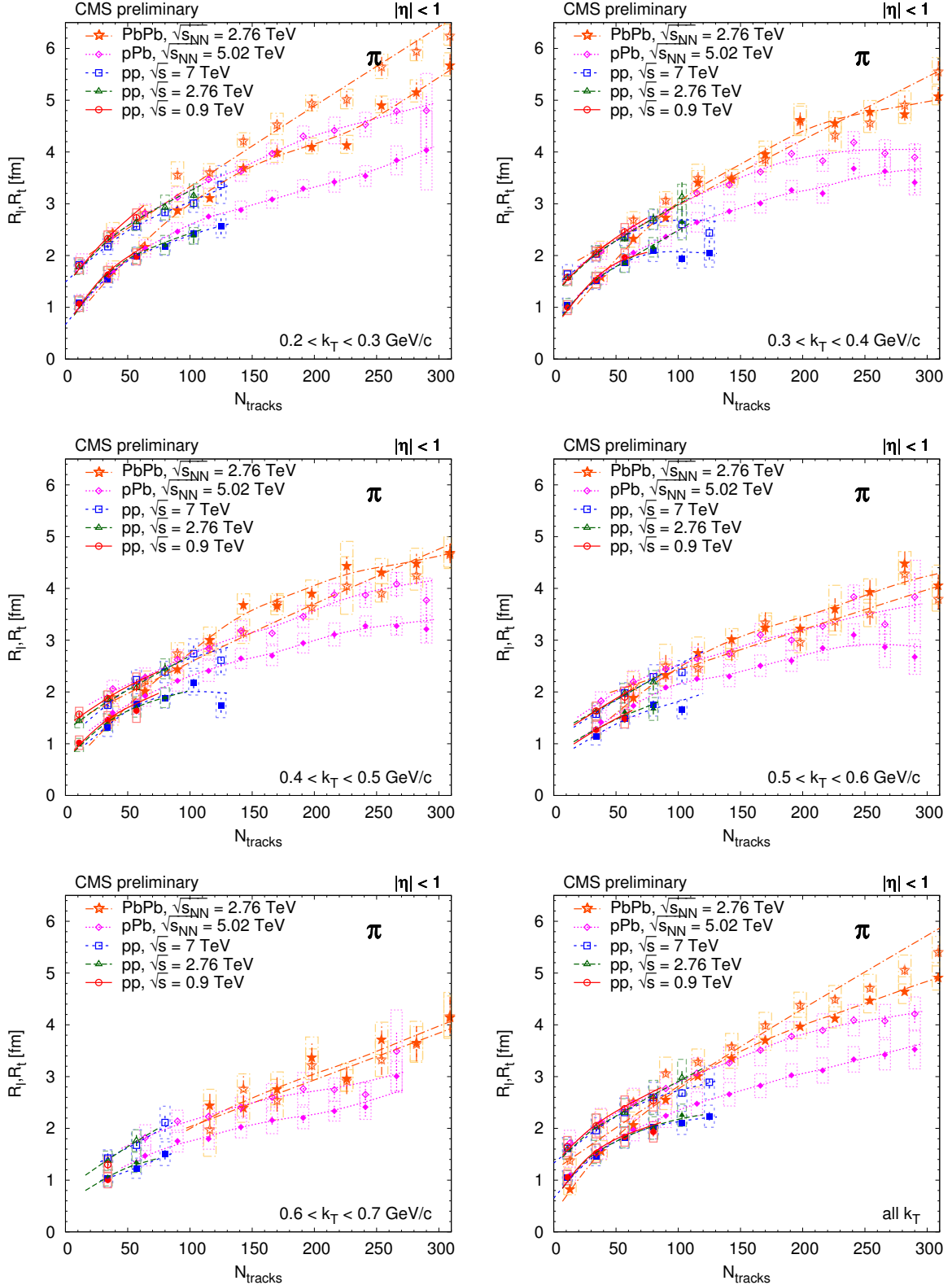


Figure 18:  $N_{\text{tracks}}$  dependence of the two-dimensional pion radii ( $R_l$  – open symbols,  $R_t$  – closed symbols), shown here for several  $k_T$  bins, for all studied reactions. Lines are drawn to guide the eye.

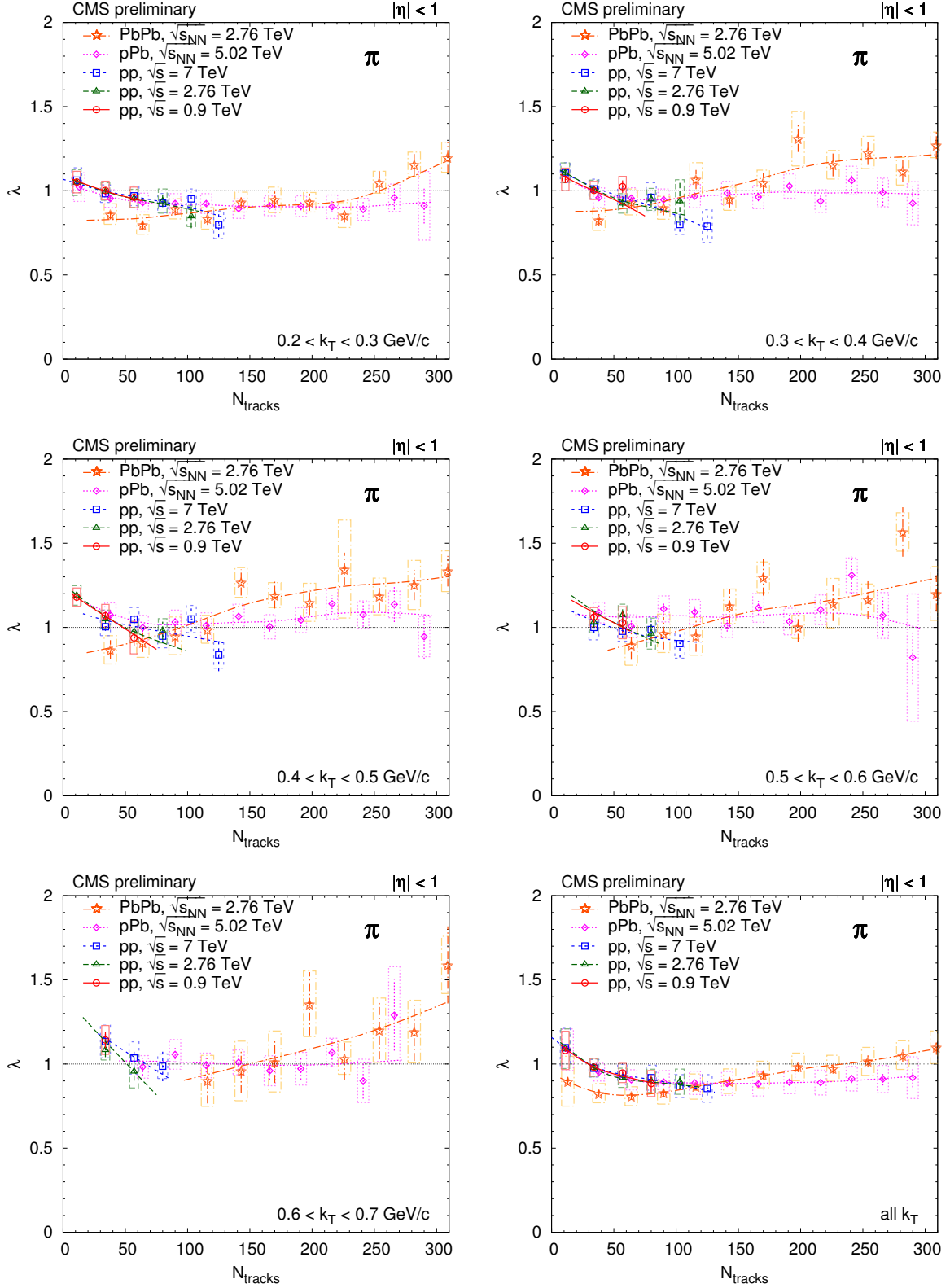


Figure 19:  $N_{\text{tracks}}$  dependence of the two-dimensional pion chaoticity parameter, shown here for several  $k_{\text{T}}$  bins, for all studied reactions. Lines are drawn to guide the eye.

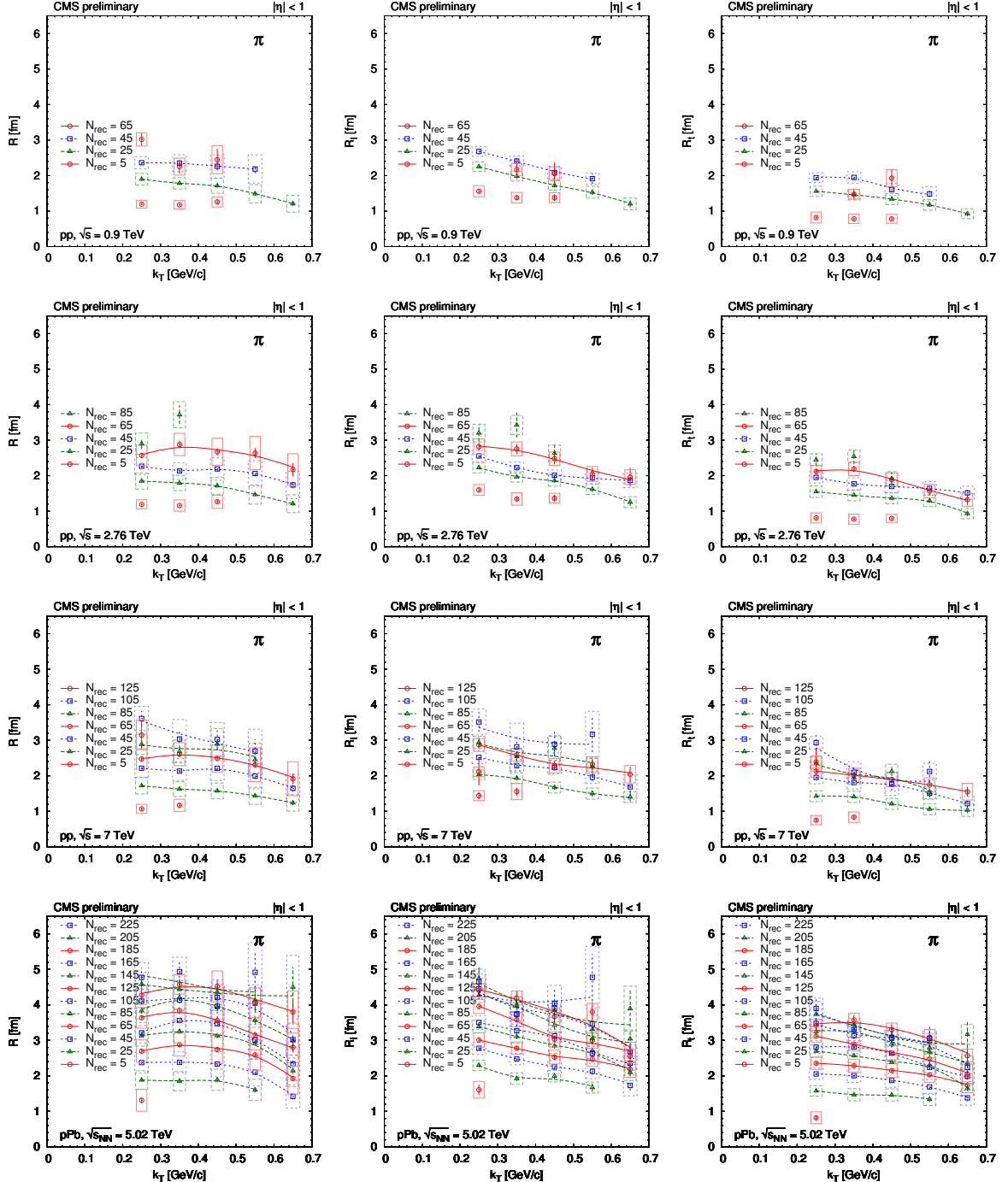


Figure 20:  $k_T$  dependence of one- ( $R$ ) and two-dimensional radii ( $R_l$ ,  $R_t$ ), shown here for several  $N_{\text{rec}}$  bins, for all systems studied. Lines are drawn to guide the eye.

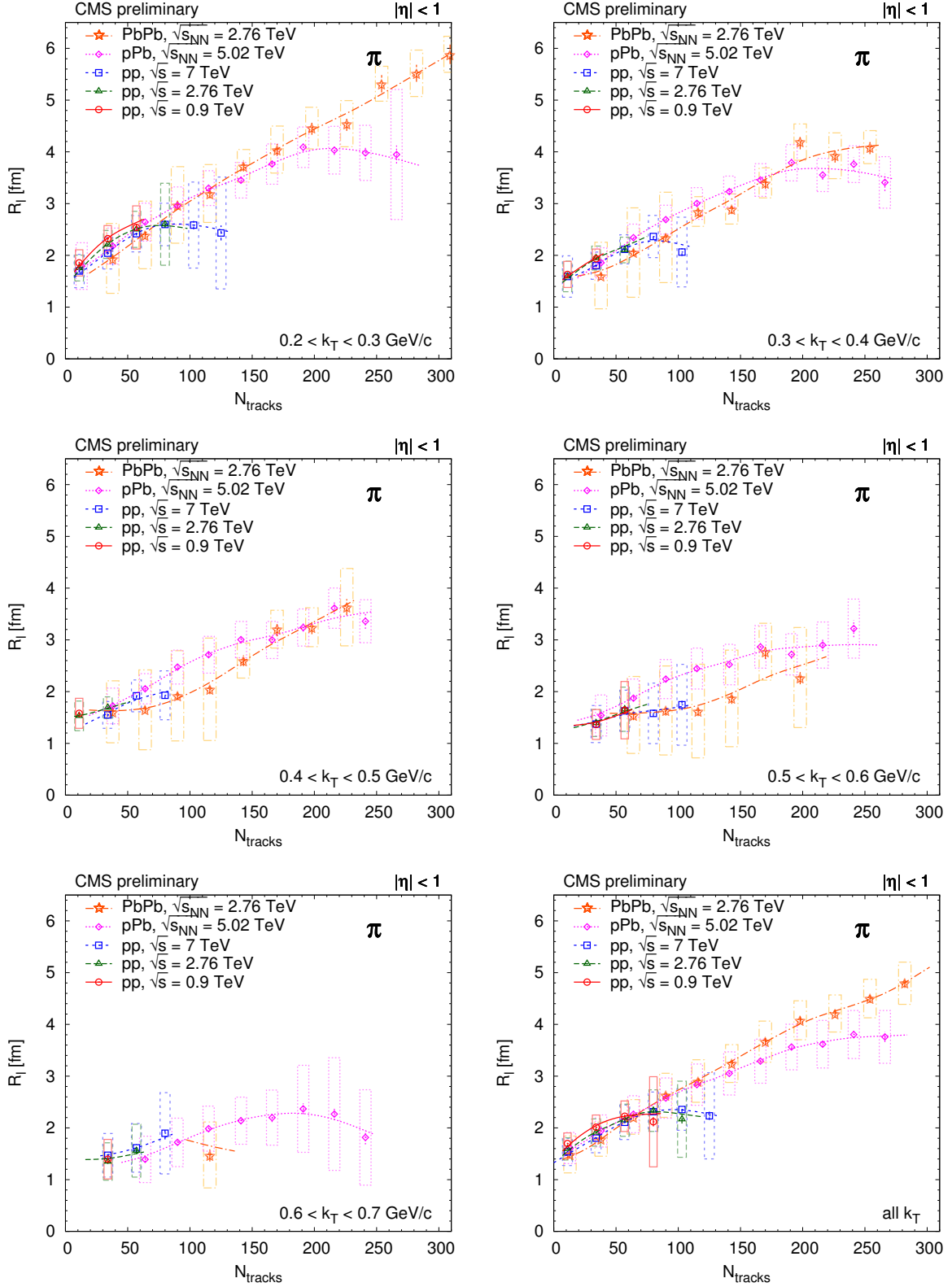


Figure 21:  $N_{\text{tracks}}$  dependence of the three-dimensional pion radii (the  $R_l$  component), shown here for several  $k_T$  bins, for all studied reactions. Lines are drawn to guide the eye.

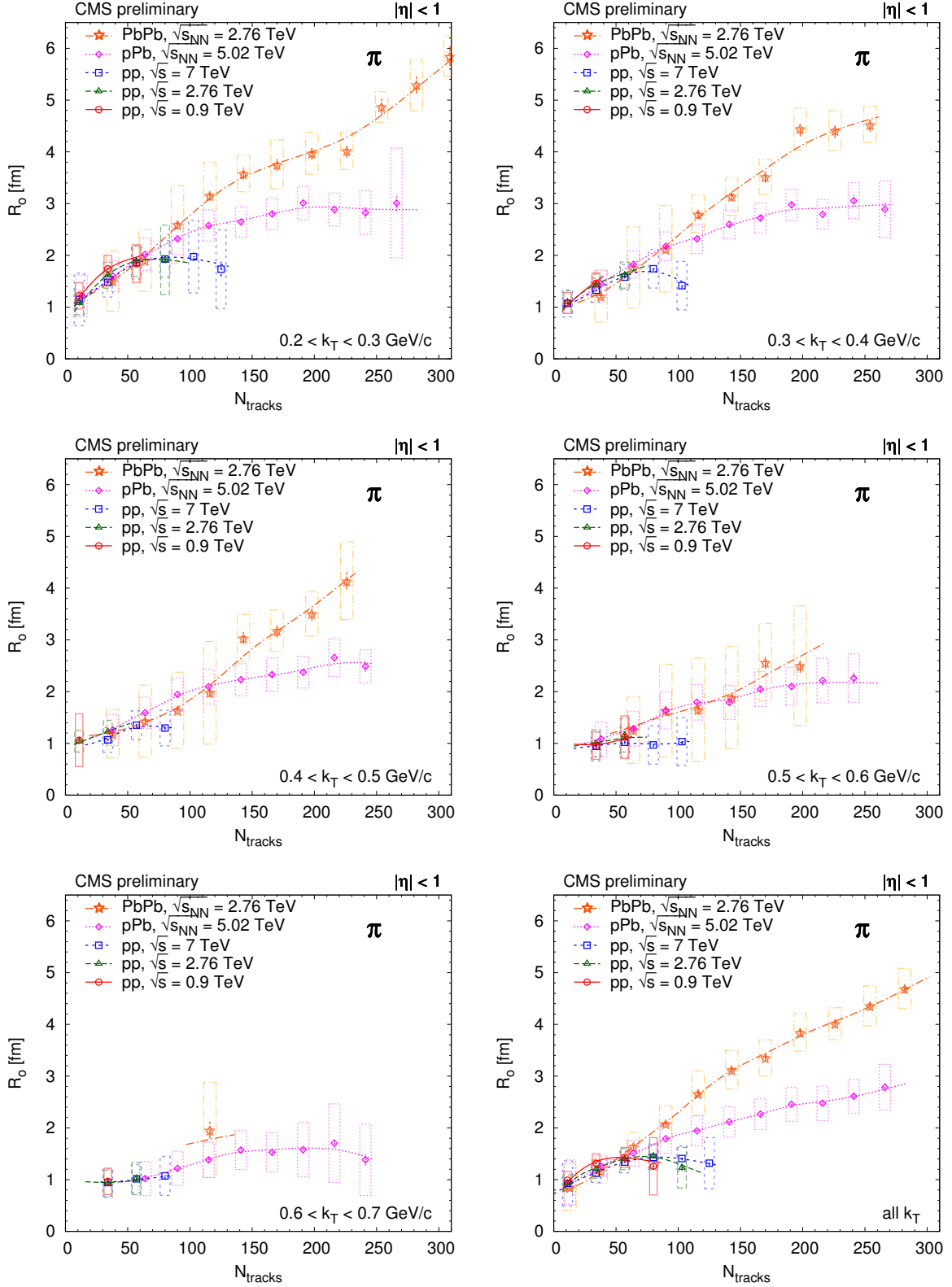


Figure 22:  $N_{\text{tracks}}$  dependence of the three-dimensional pion radii (the  $R_o$  component), shown here for several  $k_T$  bins, for all studied reactions. Lines are drawn to guide the eye.

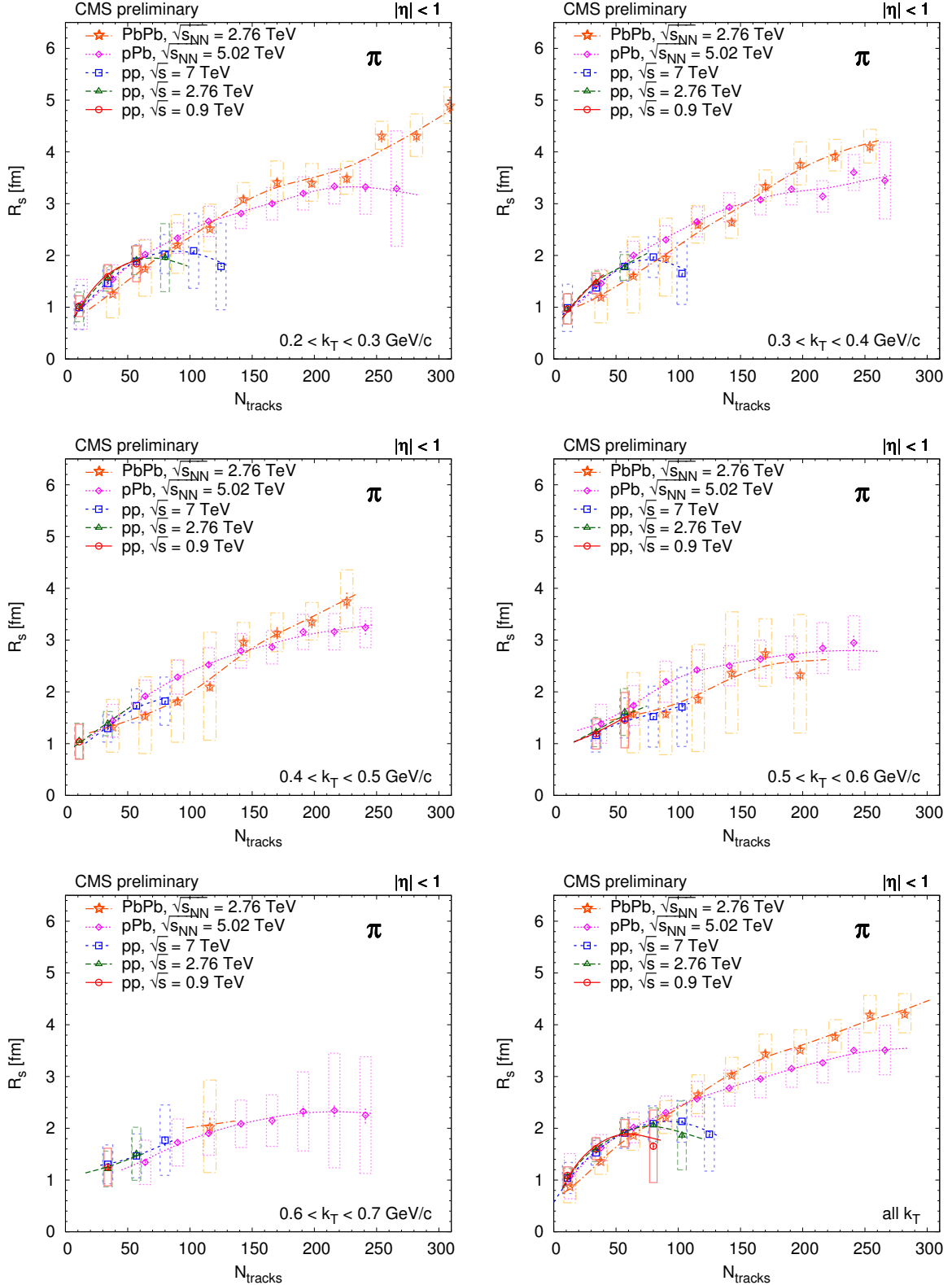


Figure 23:  $N_{\text{tracks}}$  dependence of the three-dimensional pion radii (the  $R_s$  component), shown here for several  $k_T$  bins, for all studied reactions. Lines are drawn to guide the eye.

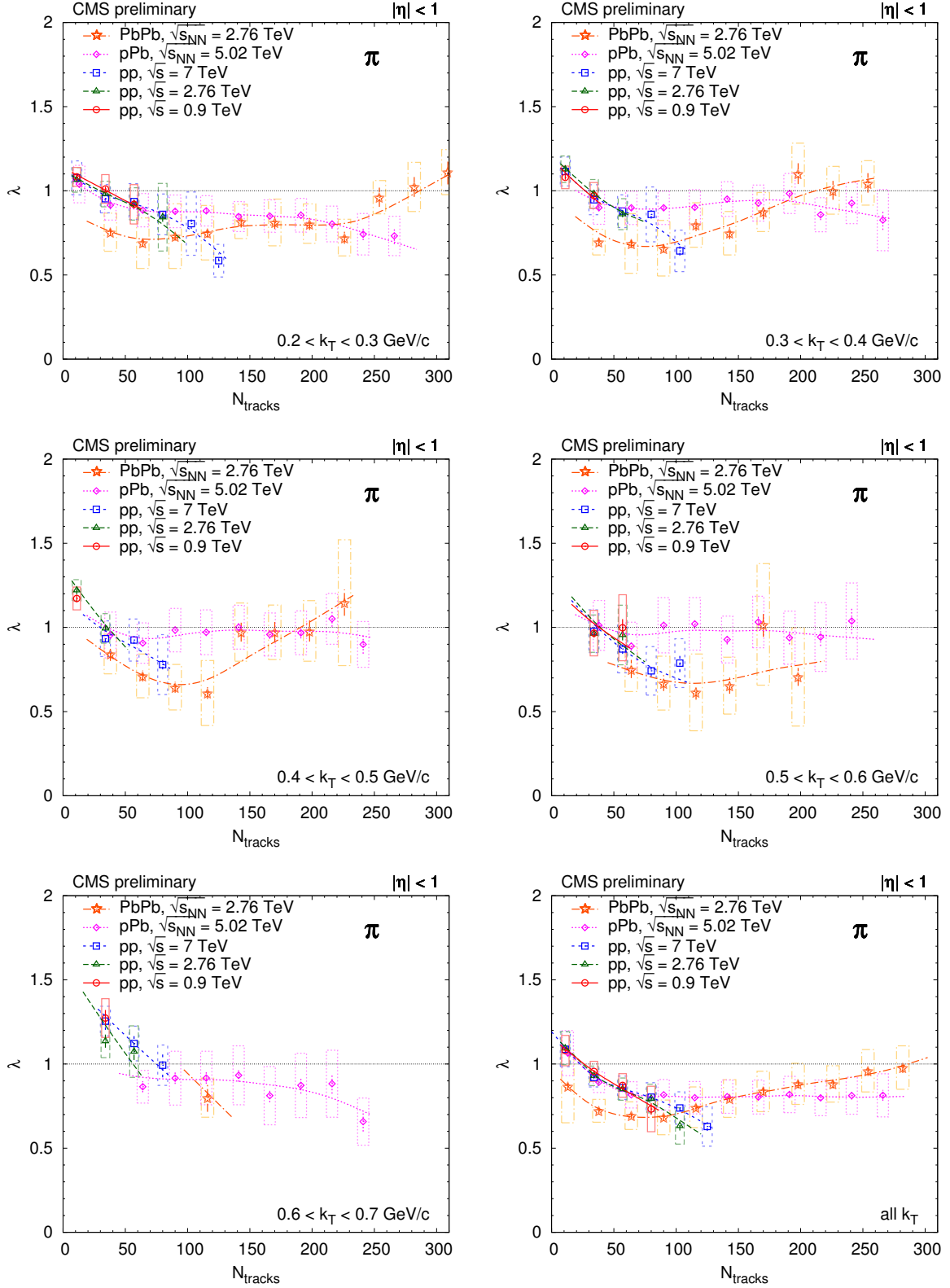


Figure 24:  $N_{\text{tracks}}$  dependence of the three-dimensional pion chaoticity parameter, shown here for several  $k_T$  bins, for all studied reactions. Lines are drawn to guide the eye.

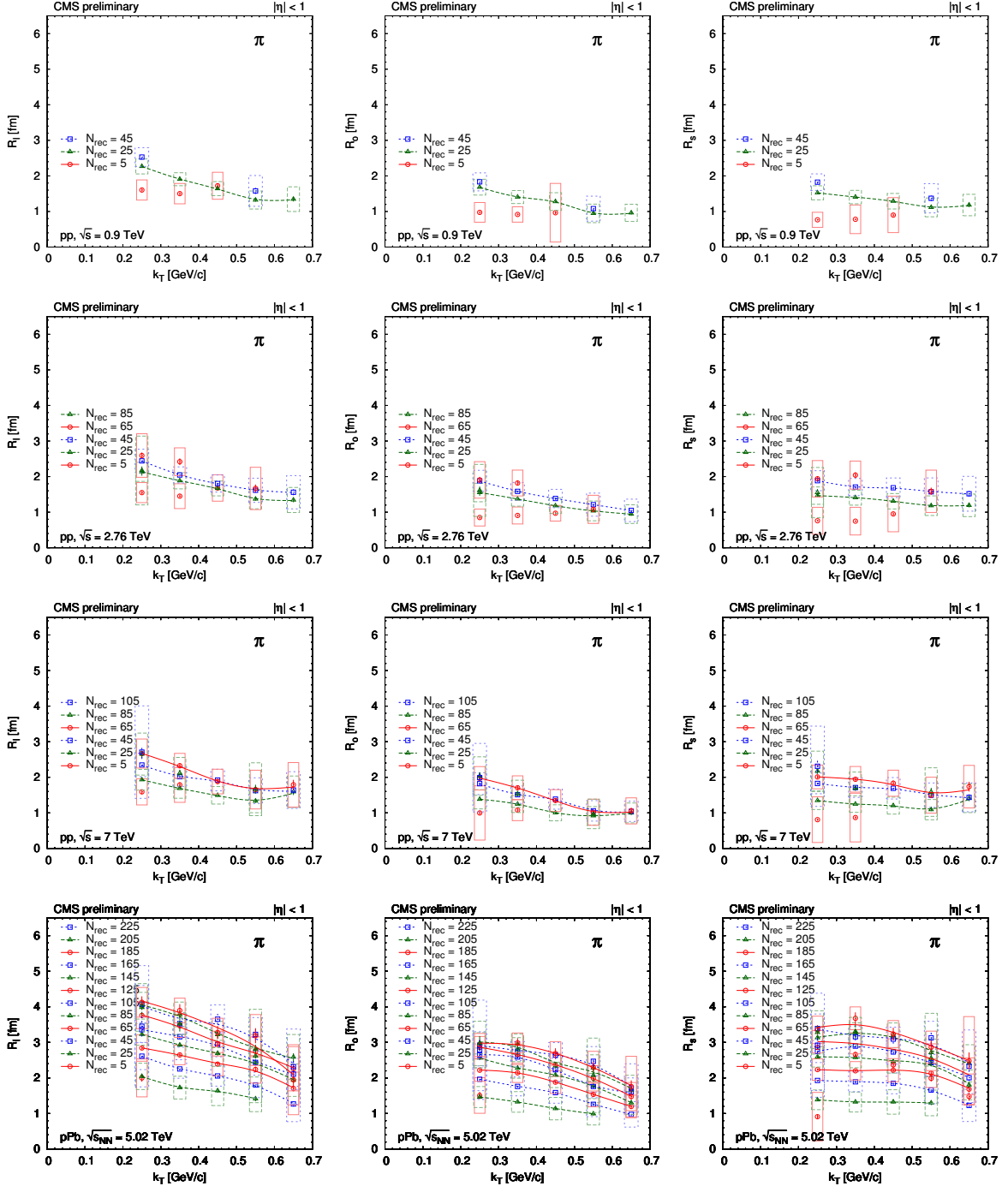


Figure 25:  $k_T$  dependence of three-dimensional radii ( $R_l$ ,  $R_o$ ,  $R_s$ ), shown here for several  $N_{\text{rec}}$  bins, for all systems studied. Lines are drawn to guide the eye.

### 3.1 Scaling

The extracted radii are in the range 1–5 fm, reaching highest values for very high multiplicity pPb, also for similar multiplicity PbPb collisions, and decrease with increasing  $k_T$ . By fitting the radii with a product of two independent functions of  $N_{\text{tracks}}$  and  $k_T$ , the dependences on multiplicity and pair momentum were shown to factorize. In some cases the radii are less sensitive to the type of the colliding system and center-of-mass energy. Radius parameters as a function of  $N_{\text{tracks}}$  at  $k_T = 0.45 \text{ GeV}/c$  are shown in the left columns of Figs. 26 and 27. We have also fitted and plotted the following  $R_{\text{param}}$  functions

$$R_{\text{param}}(N_{\text{tracks}}, k_T) = [a^2 + (b N_{\text{tracks}}^\beta)^2]^{1/2} \cdot (0.2 \text{ GeV}/c/k_T)^\gamma, \quad (11)$$

where the minimal radius  $a$  and the exponents  $\gamma$  of  $k_T$  are kept the same for a given radius component, for all collision types. This choice of parametrization is based on previous results [38]. The minimal radius can be connected to the size of the proton, while the power-law dependence on  $N_{\text{tracks}}$  is often attributed to the freeze-out density of hadrons. The ratio of radius parameter and the value of the above parametrization at  $k_T = 0.45 \text{ GeV}/c$  as a function  $k_T$  is shown in the right columns of Figs. 26 and 27. The obtained parameter values are listed in Table 3.

## 4 Conclusions

The characteristics of the one-, two-, and three-dimensional two-particle correlation functions in various center-of-mass energy pp, pPb, and peripheral PbPb collisions were studied as a function of the transverse pair momentum  $k_T$  and of the charged-particle multiplicity  $N_{\text{tracks}}$  of the event. Charged pions and kaons at low  $p_T$  and in laboratory pseudorapidity  $|\eta| < 1$  were identified via their energy loss in the silicon tracker. The correlation functions were corrected for the Coulomb interaction between particles. The contributions from other, correlated particle emissions (mini-jets, multi-body resonance decays) were also subtracted. The obtained distributions could be fit by an exponential parametrization in the relative momentum of the particle pair, both in one- and in multi-dimensions. This choice is a special case of the broader class of stretched exponential parametrization with  $\alpha = 1$ , and points to a Cauchy (Lorentz) type source distribution. It has long power-law tails, in contrast with the often used Gaussian functional form.

The extracted exponential radii for pions increase with increasing  $N_{\text{tracks}}$  for all systems and

Table 3: Values of the fit parameters.

Radius	$a$ [fm]	pp		pPb		PbPb		$\gamma$
		$b$ [fm]	$\beta$	$b$ [fm]	$\beta$	$b$ [fm]	$\beta$	
$R$	1.03	0.28	0.52	0.31	0.49	0.25	0.56	0.18
$R_l$	1.20	0.58	0.37	0.53	0.41	0.40	0.48	0.39
$R_t$	0.01	0.45	0.38	0.43	0.41	0.26	0.55	0.29
$R_l$	1.32	0.77	0.28	0.46	0.43	0.19	0.61	0.51
$R_o$	0.11	0.90	0.20	0.56	0.37	0.21	0.61	0.73
$R_s$	0.01	0.44	0.36	0.34	0.45	0.16	0.60	0.22

center-of-mass energies studied, for one, two, and three dimensions alike. Their values are in the range 1–5 fm, reaching highest values for very high multiplicity pPb, also for similar multiplicity PbPb collisions. The  $N_{\text{tracks}}$  dependence of  $R_l$  and  $R_t$  is similar for pp and pPb in all  $k_T$  bins, and that similarity also applies to peripheral PbPb if  $k_T > 0.4 \text{ GeV}/c$ . In general there is an ordering,  $R_l > R_t$ , and  $R_l > R_s > R_o$ , thus the pp and pPb source is elongated in the beam direction. In the case of peripheral PbPb the source is quite symmetric, and shows a slightly different  $N_{\text{tracks}}$  dependence, with largest differences for  $R_t$  and  $R_o$ , while there is a good agreement for  $R_l$  and  $R_s$ . The most visible divergence between pp, pPb and PbPb is seen in  $R_o$  that could point to the differing lifetime of the created systems in those collisions.

The kaon radii also show some increase with  $N_{\text{tracks}}$ , although its magnitude is smaller than that for pions. Longer lived resonances and rescattering may play a role here. The pion radii decrease with increasing  $k_T$ . The dependence of the radii on the multiplicity and  $k_T$  factorizes and in some cases appears to be less sensitive to the type of the colliding system and center-of-mass energy. The similarities observed in the  $N_{\text{tracks}}$  dependence may point to a common critical hadron density in pp, pPb, and peripheral PbPb collisions, since the present correlation technique measures the characteristic size of the system near the time of the last interactions.

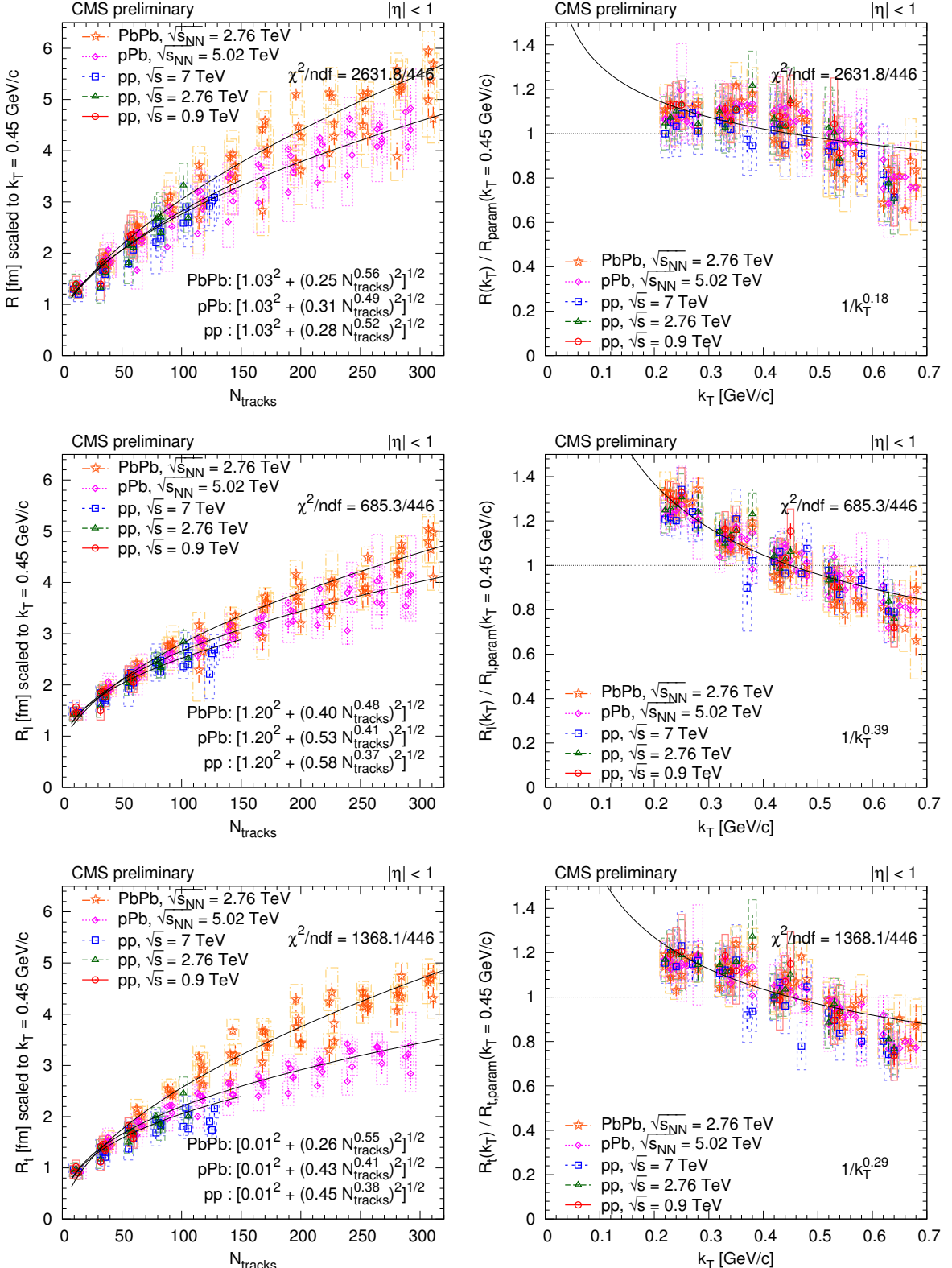


Figure 26: Left: radius parameters as a function of  $N_{\text{tracks}}$  scaled to  $k_T = 0.45 \text{ GeV}/c$  with help of the parametrization  $R_{\text{param}}$  (Eq. (11)). Right: ratio of the radius parameter and the value of the parametrization  $R_{\text{param}}$  (Eq. (11)) at  $k_T = 0.45 \text{ GeV}/c$  as a function  $k_T$ . (Points were shifted to left and to right with respect to the center of the  $k_T$  bin for better visibility.) Upper row:  $R$  from the one-dimensional ( $q_{\text{inv}}$ ) analysis. Middle row:  $R_l$  from the two-dimensional ( $q_l, q_t$ ) analysis. Bottom row:  $R_t$  from the two-dimensional ( $q_l, q_t$ ) analysis. Fit results are indicated in the figures, for details see text.

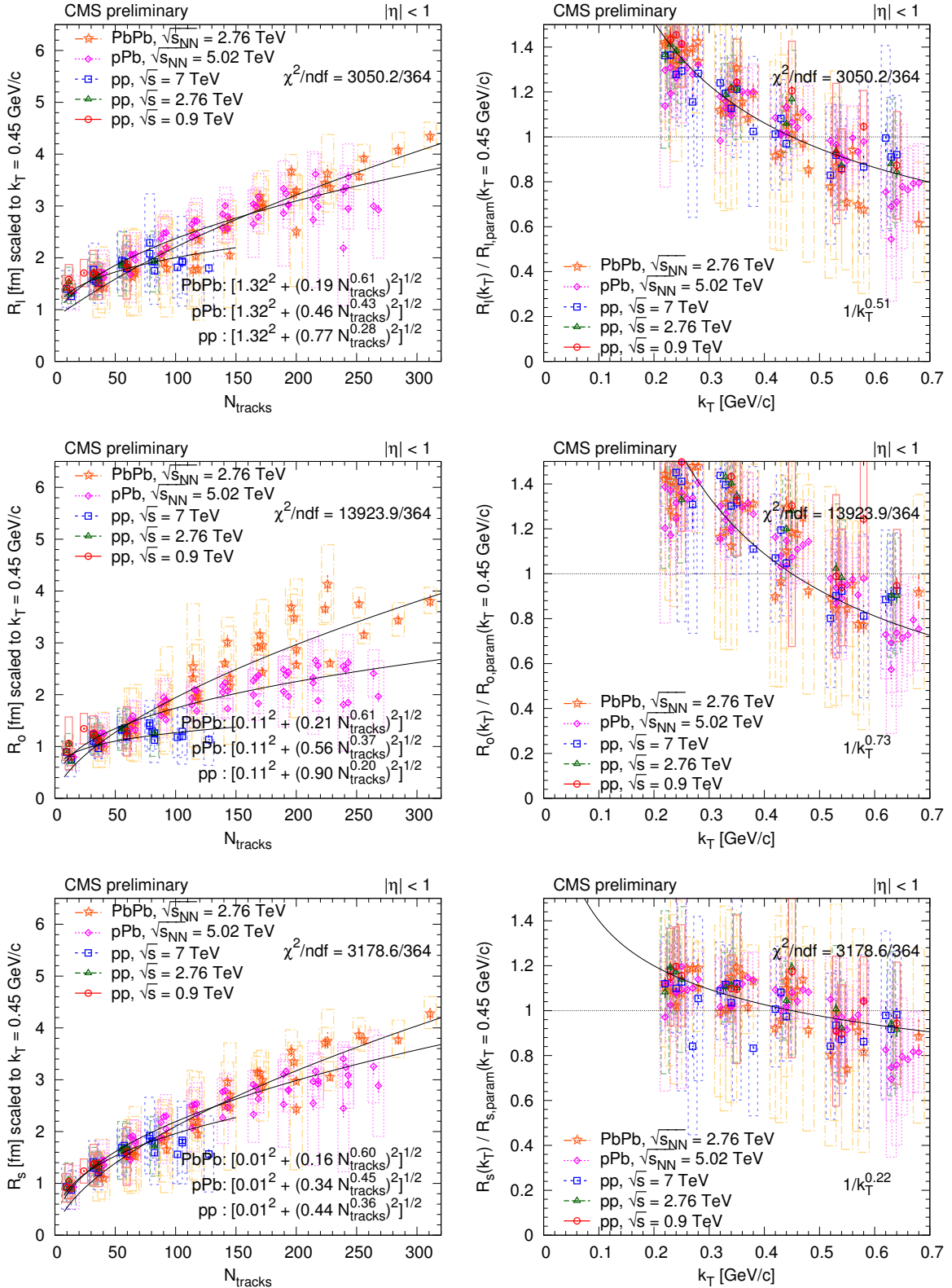


Figure 27: Left: radius parameters as a function of  $N_{\text{tracks}}$  scaled to  $k_T = 0.45 \text{ GeV}/c$  with help of the parametrization  $R_{\text{param}}$  (Eq. (11)). Right: ratio of the radius parameter and the value of the parametrization  $R_{\text{param}}$  (Eq. (11)) at  $k_T = 0.45 \text{ GeV}/c$  as a function  $k_T$ . (Points were shifted to left and to right with respect to the center of the  $k_T$  bin for better visibility.) Radii from the three-dimensional ( $q_1, q_0, q_s$ ) analysis are shown, from top to bottom:  $R_l$ ,  $R_o$ ,  $R_s$ . Fit results are indicated in the figures, for details see text.

## References

- [1] B. Erazmus et al., "Nuclear interferometry from low-energy to ultrarelativistic nucleus-nucleus collisions", (1996). SUBATECH-96-03.
- [2] CMS Collaboration, "Measurement of Bose-Einstein correlations with first CMS data", *Phys. Rev. Lett.* **105** (2010) 032001, doi:10.1103/PhysRevLett.105.032001, arXiv:1005.3294.
- [3] CMS Collaboration, "Measurement of Bose-Einstein Correlations in  $pp$  Collisions at  $\sqrt{s} = 0.9$  and 7 TeV", *JHEP* **05** (2011) 029, doi:10.1007/JHEP05(2011)029, arXiv:1101.3518.
- [4] STAR Collaboration, "Pion femtoscopy in  $p^+p$  collisions at  $\sqrt{s} = 200$  GeV", *Phys. Rev. C* **83** (2011) 064905, doi:10.1103/PhysRevC.83.064905, arXiv:1004.0925.
- [5] ALICE Collaboration, "Femtoscopy of  $pp$  collisions at  $\sqrt{s} = 0.9$  and 7 TeV at the LHC with two-pion Bose-Einstein correlations", *Phys. Rev. D* **84** (2011) 112004, doi:10.1103/PhysRevD.84.112004, arXiv:1101.3665.
- [6] ALICE Collaboration, "Two-pion Bose-Einstein correlations in central Pb-Pb collisions at  $\sqrt{s_{NN}} = 2.76$  TeV", *Phys. Lett. B* **696** (2011) 328–337, doi:10.1016/j.physletb.2010.12.053, arXiv:1012.4035.
- [7] ALICE Collaboration, "Two and Three-Pion Quantum Statistics Correlations in Pb-Pb Collisions at  $\sqrt{s_{NN}} = 2.76$  TeV at the LHC", *Phys. Rev. C* **89** (2014) 024911, doi:10.1103/PhysRevC.89.024911, arXiv:1310.7808.
- [8] ALICE Collaboration, "Freeze-out radii extracted from three-pion cumulants in  $pp$ ,  $p$ -Pb and Pb-Pb collisions at the LHC", arXiv:1404.1194. Submitted to *Eur. Phys. J. C*.
- [9] PHENIX Collaboration, "Charged kaon interferometric probes of space-time evolution in Au+Au collisions at  $\sqrt{s_{NN}} = 200$  GeV", *Phys. Rev. Lett.* **103** (2009) 142301, doi:10.1103/PhysRevLett.103.142301, arXiv:0903.4863.
- [10] ALICE Collaboration, "Charged kaon femtoscopic correlations in  $pp$  collisions at  $\sqrt{s} = 7$  TeV", *Phys. Rev. D* **87** (2013) 052016, doi:10.1103/PhysRevD.87.052016, arXiv:1212.5958.
- [11] ALICE Collaboration, " $K_s^0 - \bar{K}_s^0$  correlations in  $pp$  collisions at  $\sqrt{s} = 7$  TeV from the LHC ALICE experiment", *Phys. Lett. B* **717** (2012) 151–161, doi:10.1016/j.physletb.2012.09.013, arXiv:1206.2056.
- [12] CMS Collaboration, "The CMS experiment at the CERN LHC", *JINST* **3** (2008) S08004, doi:10.1088/1748-0221/3/08/S08004.
- [13] CMS Collaboration, "Study of the inclusive production of charged pions, kaons, and protons in  $pp$  collisions at  $\sqrt{s} = 0.9, 2.76$ , and 7 TeV", *Eur. Phys. J. C* **72** (2012) 2164, doi:10.1140/epjc/s10052-012-2164-1, arXiv:1207.4724.
- [14] CMS Collaboration, "Study of the production of charged pions, kaons, and protons in  $p$ Pb collisions at  $\sqrt{s_{NN}} = 5.02$  TeV", arXiv:1307.3442. Accepted by *Eur. Phys. J. C*.
- [15] CMS Collaboration, "Transverse momentum and pseudorapidity distributions of charged hadrons in  $pp$  collisions at  $\sqrt{s} = 0.9$  and 2.36 TeV", *JHEP* **02** (2010) 041, doi:10.1007/JHEP02(2010)041, arXiv:1002.0621.

- [16] F. Siklér, “Low  $p_T$  Hadronic Physics with CMS”, *Int. J. Mod. Phys. E* **16** (2007) 1819, doi:10.1142/S0218301307007052, arXiv:physics/0702193.
- [17] CMS Collaboration, “Transverse-momentum and pseudorapidity distributions of charged hadrons in pp collisions at  $\sqrt{s} = 7$  TeV”, *Phys. Rev. Lett.* **105** (2010) 022002, doi:10.1103/PhysRevLett.105.022002, arXiv:1005.3299.
- [18] F. Siklér, “Study of clustering methods to improve primary vertex finding for collider detectors”, *Nucl. Instrum. Meth. A* **621** (2010) 526, doi:10.1016/j.nima.2010.04.058, arXiv:0911.2767.
- [19] T. Sjöstrand, S. Mrenna, and P. Z. Skands, “PYTHIA 6.4 physics and manual”, *JHEP* **05** (2006) 026, doi:10.1088/1126-6708/2006/05/026, arXiv:hep-ph/0603175.
- [20] W.-T. Deng, X.-N. Wang, and R. Xu, “Hadron production in p+p, p+Pb, and Pb+Pb collisions with the HIJING 2.0 model at energies available at the CERN Large Hadron Collider”, *Phys. Rev. C* **83** (2011) 014915, doi:10.1103/PhysRevC.83.014915, arXiv:1008.1841.
- [21] R. Xu, W.-T. Deng, and X.-N. Wang, “Nuclear modification of high- $p_T$  hadron spectra in p+A collisions at LHC”, *Phys. Rev. C* **86** (2012) 051901, doi:10.1103/PhysRevC.86.051901, arXiv:1204.1998.
- [22] I. Lokhtin et al., “Heavy ion event generator HYDJET++ (HYDrodynamics plus JETs)”, *Comput. Phys. Commun.* **180** (2009) 779–799, doi:10.1016/j.cpc.2008.11.015, arXiv:0809.2708.
- [23] Particle Data Group, J. Beringer et al., “Review of Particle Physics”, *Phys. Rev. D* **86** (2012) 010001, doi:10.1103/PhysRevD.86.010001.
- [24] F. Siklér, “A parametrisation of the energy loss distributions of charged particles and its applications for silicon detectors”, *Nucl. Instrum. Meth. A* **691** (2012) 16, doi:10.1016/j.nima.2012.06.064, arXiv:1111.3213.
- [25] T. Csörgő, S. Hegyi, and W. Zajc, “Bose-Einstein correlations for Levy stable source distributions”, *Eur. Phys. J. C* **36** (2004) 67–78, doi:10.1140/epjc/s2004-01870-9, arXiv:nucl-th/0310042.
- [26] T. Csörgő, S. Hegyi, and W. Zajc, “Stable Bose-Einstein correlations”, arXiv:nucl-th/0402035.
- [27] S. Pratt, “Coherence and Coulomb effects on pion interferometry”, *Phys. Rev. D* **33** (1986) 72, doi:10.1103/PhysRevD.33.72.
- [28] M. Biyajima and T. Mizoguchi, “Coulomb wave function correction to Bose-Einstein correlations”, (1994). SULDP-1994-9.
- [29] M. Bowler, “Coulomb corrections to Bose-Einstein correlations have been greatly exaggerated”, *Phys. Lett. B* **270** (1991) 69–74, doi:10.1016/0370-2693(91)91541-3.
- [30] Y. Sinyukov et al., “Coulomb corrections for interferometry analysis of expanding hadron systems”, *Phys. Lett. B* **432** (1998) 248–257, doi:10.1016/S0370-2693(98)00653-4.
- [31] D. Anchishkin, W. Zajc, and G. Zinovev, “Coulomb final state interaction in pion interferometry for the processes of high multiplicity”, arXiv:hep-ph/9512279.

- [32] C.-Y. Wong and L. Chatterjee, “Effects of final state interaction and screening on strange and heavy quark production”, *Heavy Ion Phys.* **4** (1996) 201, arXiv:hep-ph/9607316.
- [33] C.-Y. Wong and L. Chatterjee, “Effects of screening on quark - anti-quark cross-sections in quark - gluon plasma”, *Z. Phys. C* **75** (1997) 523, doi:10.1007/s002880050496, arXiv:hep-ph/9604224.
- [34] M. Abramowitz and I. A. Stegun, “Handbook of Mathematical Functions with Formulas, Graphs, and Mathematical Tables”. Dover Publications, New York, 1964.
- [35] PHOBOS Collaboration, “System size dependence of cluster properties from two-particle angular correlations in Cu+Cu and Au+Au collisions at  $\sqrt{s_{NN}} = 200 \text{ GeV}$ ”, *Phys. Rev. C* **81** (2010) 024904, doi:10.1103/PhysRevC.81.024904, arXiv:0812.1172.
- [36] CMS Collaboration, “Observation of Long-Range Near-Side Angular Correlations in Proton-Proton Collisions at the LHC”, *JHEP* **09** (2010) 091, doi:10.1007/JHEP09(2010)091, arXiv:1009.4122.
- [37] CMS Collaboration, “Observation of long-range near-side angular correlations in proton-lead collisions at the LHC”, *Phys. Lett. B* **718** (2013) 795–814, doi:10.1016/j.physletb.2012.11.025, arXiv:1210.5482.
- [38] M. Lisa, “Femtoscopy in heavy ion collisions: Wherefore, whence, and whither?”, *AIP Conf. Proc.* **828** (2006) 226–237, doi:10.1063/1.2197421, arXiv:nucl-ex/0512008.